Bayesian operational modal analysis with multiple setups and multiple (possibly close) modes

Zuo Zhu[1], Siu-Kui Au[2], Binbin Li[3*], Yan-Long Xie[3]

[1]Institute for Risk and Uncertainty and School of Engineering, University of Liverpool, United Kingdom
[2] School of Civil and Environmental Engineering, Nanyang Technological University, Singapore
[3]ZJU-UIUC Institute, Zhejiang University, China
[*]Corresponding author. E-mail address: bbl@zju.edu.cn

Abstract

Operational modal analysis (OMA) is increasingly applied to identify the modal properties of a constructed structure for its high economy in implementation. Though great achievement has been made in OMA, it is still challenging in the scenario of multiple setup data with close modes, due to the need to assemble the global mode shapes and the intervention of close modes, especially when the data quality is low in some setups. A Bayesian approach is developed in this paper to compute the most probable value (MPV) of modal parameters incorporating data from multiple setups and multiple (possibly close) modes. It employs an expectation-maximisation algorithm which admits an analytical update of modal parameters except the frequencies and damping ratios, thus allowing an efficient computation of the MPV, usually in the order of tens of seconds for each frequency band even when there are a large number of degrees of freedom and long data. A comprehensive study based on synthetic and field test data is presented to illustrate the performance of the proposed algorithm. Comparing with three existing algorithms, it shows the quality of the identified global mode shape is good and insensitive to the method used when the data quality is consistently high in all setups; However, only the proposed Bayesian approach yields consistently reasonable results when the data quality is low in some setups.

Keywords

Operational modal analysis; field test; Bayesian inference; BAYOMA; Expectation-Maximisation; multiple setups; close modes

1. Introduction

Operational modal analysis (OMA) [1–3] aims at identifying structural modal properties (natural frequencies, damping ratios, mode shapes, etc.) using ambient vibration data. The input excitation is not measured in ambient vibration test but is assumed to be broadband random. This allows the data to be collected economically in the operational condition of the structure without much intervention, which makes OMA popular in implementation. An increasing number of ambient vibration tests have been performed in the last few decades, see, e.g., [4–9]. The identified modal parameters are often demanded in downstream applications, e.g., damage detection [10–12], model updating [13–15] and structural health monitoring [16–18].

In OMA, the identified mode shapes can provide insights into the nature of modes through the relative motion of the measured degrees of freedom (DOFs). A higher spatial resolution of mode shape can only be achieved by increasing the number of measured locations. In full-scale field tests, however, many situations exist where there are a large number of DOFs to be measured but only a limited number of sensors are available due to, e.g., limited instrumentation budget or manpower. This implies that the DOFs of interest cannot be measured synchronously together in a single setup. A common feasible strategy is to conduct multiple setups, with each setup covering different parts of the structure. Different setups need to share some reference DOFs in common so that the 'global mode shape' covering all measured DOFs can be assembled by virtue of the common information among the setups. Obtaining high-resolution mode shapes is the main target of multiple setup test. According to the order of mode shape assembly prior or posterior to the identification, the modal identification approaches can be categorised into either pre- or post-identification, and they are briefly reviewed as follow.

Conventionally, post-identification approach is employed to produce the global mode shapes. The modal parameters in each setup are identified individually using the corresponding data. The global mode shape is then 'assembled' or 'glued' from the 'local mode shapes' in different setups. Local least squares method [1] provides a heuristic way for gluing mode shapes. It requires one to select a reference setup first. The mode shape in any other setup is scaled so that the mode shape values at the reference DOFs best fit their counterparts in the reference setup in a least squares sense. The quality of results, however, depends critically on the choice of the reference setup [1]. If the quality of identified mode shape in the reference setup is poor (e.g., significant disagreement of mode shape values at the reference DOFs with other setups),

the assembled mode shape will be of poor quality, often appearing as physically unreasonable. Global least squares method [19] eliminates the choice of reference setup by fitting the local mode shapes in different setups simultaneously in an overall sense through a single objective function, subjected to scaling constraint of the global mode shape. It has been found to give reasonable results in many full-scale field tests [4,6,20,21]. Conventional procedures put equal weight on different setups, although intuitively the setups with poor data quality should have less influence on the assembled mode shape since the local mode shapes identified in these problematic setups are less reliable. In Section 14.3.6 of [1], a strategy, based on well-separated modes with high signal-to-noise (s/n) ratio, is suggested to place the weights proportional to the modal s/n ratio of the setups. In addition, the least squares methods only make use of the information of local mode shapes and they ignore other modal properties, which may be important when the data quality in some setups is poor.

Pre-identification approach is also available to assemble the global mode shapes. The basic idea is to merge datasets from multiple setups and then use the combined dataset for modal identification as if it is from a single setup based on certain modelling assumptions. Since the ambient excitation can differ from one setup to another, the data in different setups must be scaled properly before merging to a global dataset. In [22], the data-merging strategy is applied to stochastic subspace identification (SSI) method for multiple setup measurements where the Hankel matrices of the roving sensor data are normalised by their counterparts of the reference sensor data. This method was later generalised to a modular SSI method [23]. In [24], a frequency-domain method was proposed by merging data power spectral density (PSD) from multiple setups before modal identification. Compared to the post-identification approach, the pre-identification is less demanding on identification as it allows one to use essentially a single setup algorithm. This is at the expense of assuming that all modal parameters to be time-invariant in all setups, which could be a major source of modelling error.

A Bayesian method based on the Fast Fourier Transform (FFT) of OMA data was developed for modal identification incorporating multiple setup data [25]. Allowing modal properties other than mode shapes to vary in different setups, it provides a fundamental means to process the information in the multiple measurements and make inference for the modal properties in a manner strictly consistent with modelling assumptions and probability logic. The comparisons between the Bayesian and post-identification methods [25,26] revealed that when the data quality is high in all setups the quality of global mode shapes is high and insensitive to the choice of method, e.g., be it local or global (least squares), Bayesian or non-Bayesian.

In the general case, however, Bayesian method tends to be more robust to data quality, giving reasonable mode shapes in cases with low data quality where least squares methods deliver spurious results.

One critical issue with the Bayesian method is computational effort. The determination of modal parameters involves numerical optimisation of the posterior probability density function (PDF) which is a nontrivial nonlinear multi-dimensional function of the modal parameters. A fast algorithm has been developed in the previous work [25], allowing the modal parameters to be determined efficiently even for a large number of measured DOFs. The algorithm, however, is only applicable for well-separated modes where one can select a frequency band around the natural frequency of interest and the contribution of other modes can be ignored within the band. While well-separated modes are typical, close modes are often found in structures (e.g., symmetrical structure [27], long bridges [5,6,28,29] and high-rise buildings [30–32]). Fast Bayesian algorithm for the general case of multiple (possibly close) modes with multiple setups has not been developed yet, as the case of single setup is already challenging [33], demanding advanced linear algebra and iterations to resolve measured mode shapes that are not necessarily orthogonal and modal excitations (hence response) that can be coherent. As a sequel to the development, this paper proposes a fast algorithm for computing the most probable value (MPV) of modal properties. Adopting a different route from [33], the proposed algorithm is based on Expectation-Maximisation (EM) algorithm and leverages on the discovery of special mathematical structure of the problem. A recent application of EM has led to a promising algorithm in the case of single setup [34].

This paper is organised as follow. Bayesian formulation of OMA based on FFT of multiple-setup data is first reviewed in Section 2. The EM algorithm and its variant parabolic EM (P-EM) are introduced in Section 3. Analytical investigation is performed in Section 4 so that one can leverage on the power of P-EM to solve the multiple mode multiple setup problem, resulting in an iterative algorithm where different groups of modal parameters are updated semi-analytically in turn and where the likelihood function will increase as guaranteed by the EM algorithm. A comprehensive study based on synthetic and field test data is presented in Section 5 to illustrate the performance of the proposed algorithm. Table 1 and Table 2 list respectively the abbreviations and notations used in this work.

Table 1 Abbreviations used in this work

Short	Long	Short	Long
BAYOMA	Bayesian Operational Modal Analysis	c.o.v.	Coefficient of Variation
DOF	Degree of Freedom	EM	Expectation-Maximisation
FDD	Frequency Domain Decomposition	FFT	Fast Fourier Transform
i.i.d.	independent and identically distributed	LLF	Log-likelihood Function
MAC	Modal Assurance Criteria	MPV	Most Probable Value
OMA	Operational Modal Analysis	PDF	Probability Density Function
P-EM	Parabolic EM	PSD	Power Spectral Density
SSI	Stochastic Subspace Identification	SV	Singular Value

Table 2 List of notations commonly used in this work

Symbol	Description	Symbol	Description
n	Number of total measured DOFs	n_r	Number of data channels in Setup r
m	Number of modes in the selected band	n_s	Number of setups
$N_f^{(r)}$	Number of FFT points in the selected band of Setup r	N_r	Number of samples per data channel in Setup r.
$L(\boldsymbol{\theta})$	LLF function	$f_i^{(r)}$	Natural frequency of Mode i in Setup r
$\zeta_i^{(r)}$	Damping ratio of Mode i in Setup r	$S_e^{(r)}$	Prediction error PSD in Setup r
$\left\{\hat{\hat{\mathbf{x}}}_j^{(r)}\right\}_{j=0}^{N_r-1}$	Measured data in Setup r; $R^{n_r\times 1}$	$\hat{F}_k^{(r)}$	One-sided scaled FFT of $\left\{\hat{\hat{\mathbf{x}}}_j^{(r)}\right\}_{j=0}^{N_r-1}$; $C^{n_r\times 1}$
$\boldsymbol{\eta}_k^{(r)}$	Scaled FFT of modal response at frequency $\mathrm{f}_k^{(r)}$ in Setup r; $C^{m\times 1}$	$\mathbf{p}_k^{(r)}=\left[p_{1k}^{(r)};\cdots;p_{mk}^{(r)}\right]$	Scaled FFT of modal force at frequency $\mathrm{f}_k^{(r)}$ in Setup r; $C^{m\times 1}$
$\mathcal{D}$	The collection of the FFTs within the selected band in all setups	$\boldsymbol{\theta}$	Modal parameters to be identified

$\mathbf{L}_r$	Selection matrix; $R^{n_r \times n}$	$\mathbf{h}_k^{(r)} = diag\left(h_{1k}^{(r)}, \cdots, h_{mk}^{(r)}\right)$	Frequency response function matrix; $C^{m \times m}$
$\mathbf{\Phi}_r = \left[\mathbf{v}_{r1}, \cdots, \mathbf{v}_{rm}\right]$	Local mode shape matrix in Setup r; $R^{n_r \times m}$	$\mathbf{\Phi} = \left[\boldsymbol{\varphi}_1 \quad \cdots \quad \boldsymbol{\varphi}_m\right]$	Global mode shape matrix; $R^{n \times m}$
$\mathbf{E}_k^{(r)}$	Theoretical PSD matrix of the data in Setup r; $C^{n_r \times n_r}$	$\mathbf{S}^{(r)}$	Modal force PSD in Setup r; $C^{m \times m}$

2. Bayesian formulation for multiple setups

The Bayesian formulation for multiple setup OMA is reviewed in this section. One may refer to [25,35] for previous work on well-separated modes and [1] for the general discussion of Bayesian Operational Modal Analysis (BAYOMA). In a multiple setup problem, different setups measure possibly different parts of the structure while sharing some reference DOFs in common. Ambient vibration data is collected from setups during different time periods. The modal parameters other than mode shapes need not be the same among setups. This accounts for the fact that the structure and environmental condition could differ (however slightly) from one setup to another, which may lead to change in the modal parameters, e.g., modal force PSDs (reflecting the ambient vibration level) and damping ratios (due to amplitude-dependent property). The data collected in different setups are related only by mode shape.

Let $\left\{\hat{\ddot{\mathbf{x}}}_j^{(r)}\right\}_{j=0}^{N_r-1}\left(n_r \times 1\right)$ be the measured ambient acceleration data in Setup r (r = 1, …, n_s; n_s is the number of setups) with n_r and N_r respectively being the number of measured DOFs and samples per data channel in this setup. The (one-sided) scaled FFT of $\left\{\hat{\ddot{\mathbf{x}}}_j^{(r)}\right\}$ at frequency $\mathrm{f}_k^{(r)} = k/\left(N_r \Delta t_r\right)\left(\mathrm{Hz}\right)$ is defined as

$$\hat{\mathcal{F}}_k^{(r)} = \sqrt{\frac{2\Delta t_r}{N_r}} \sum_{j=0}^{N_r-1} \hat{\ddot{\mathbf{x}}}_j^{(r)} e^{-2\pi \mathbf{i} jk/N_r} \tag{1}$$

where Δt_r (sec) is the sampling time interval and $\mathbf{i}^2 = -1$. Assuming linear classically damped dynamics with m dominated modes within the selected band, $\hat{\mathcal{F}}_k^{(r)}$ is modelled as

$$\hat{\mathbf{F}}_k^{(r)} = \boldsymbol{\Phi}_r \boldsymbol{\eta}_k^{(r)} + \boldsymbol{\varepsilon}_k^{(r)} \tag{2}$$

where $\boldsymbol{\Phi}_r = \left[\mathbf{v}_{r1}, \cdots, \mathbf{v}_{rm}\right] \in R^{n_r \times m}$ whose *i*-th column is the 'local mode shape' of the *i*-th mode covering only the measured DOFs in Setup *r*; $\boldsymbol{\eta}_k^{(r)}$ is the scaled FFT of modal response at frequency $\mathrm{f}_k^{(r)}$; $\boldsymbol{\varepsilon}_k^{(r)}$ denotes the scaled FFT of the prediction error (due to, e.g., data noise and modelling error) assumed to be independent and identically distributed (i.i.d.) among different measured DOFs with a constant PSD $S_e^{(r)}$ in the band. Let $\mathbf{p}_k^{(r)} = \left[p_{1k}^{(r)}; \cdots; p_{mk}^{(r)} \right] \in C^{m \times 1}$ with $p_{ik}^{(r)} \left(i = 1, \cdots, m\right)$ being the scaled FFT of the *i*-th modal force at frequency $\mathrm{f}_k^{(r)}$. Then $\boldsymbol{\eta}_k^{(r)} = \mathbf{h}_k^{(r)} \mathbf{p}_k^{(r)}$ where $\mathbf{h}_k^{(r)} = diag\left(h_{1k}^{(r)}, \cdots, h_{mk}^{(r)}\right)$ is a diagonal matrix with the *i*-th diagonal entry being the frequency response function corresponding to Mode *i* and given by (for acceleration data)

$$h_{ik}^{(r)} = \frac{1}{1 - \beta_{ik}^{(r)2} - 2\zeta_i^{(r)} \beta_{ik}^{(r)} \mathbf{i}} \qquad \beta_{ik}^{(r)} = \frac{f_i^{(r)}}{\mathrm{f}_k^{(r)}} \tag{3}$$

where $f_i^{(r)}$ and $\zeta_i^{(r)}$ are respectively the natural frequency and damping ratio of Mode *i* in Setup *r*. The modal force $\left\{\mathbf{p}_k^{(r)}\right\}$ are assumed to be stationary with a constant PSD matrix $\mathbf{S}^{(r)} \in C^{m \times m}$ within the selected band. As a standard result in stochastic processes, for long data, both $\mathbf{p}_k^{(r)}$ and $\boldsymbol{\varepsilon}_k^{(r)}$ are independent at different frequencies and follow a (circular symmetric) complex Gaussian distribution [1], i.e., $\mathbf{p}_k^{(r)} \sim CN\left(\mathbf{0}, \mathbf{S}^{(r)}\right)$ and $\boldsymbol{\varepsilon}_k^{(r)} \sim CN\left(0, S_e^{(r)} \mathbf{I}_{n_r}\right)$ where $\mathbf{I}_{n_r}$ denotes the $n_r \times n_r$ identity matrix.

Let $\boldsymbol{\varphi}_i \left(n \times 1\right)$ be the 'global mode shape' of the *i*-th mode covering all measured *n* DOFs. To relate the global mode shape to the local one in Setup *r*, a selection matrix $\mathbf{L}_r \in R^{n_r \times n}$ is defined [19], such that

$$\mathbf{v}_{ri} = \mathbf{L}_r \boldsymbol{\varphi}_i, \ i = 1, \cdots, m \tag{4}$$

The (*j*, *k*)-entry of $\mathbf{L}_r$ is 1 if the *j*-th data channel in Setup *r* measures DOF *k* in $\boldsymbol{\varphi}_i$ and zero otherwise. In the above context, the set of modal parameters $\boldsymbol{\theta}$ to be identified comprises:

$$\boldsymbol{\theta} = \left\{ \left\{ \left\{ f_i^{(r)} \right\}_{i=1}^{m}, \left\{ \zeta_i^{(r)} \right\}_{i=1}^{m}, \mathbf{S}^{(r)}, S_e^{(r)} \right\}_{r=1}^{n_s}, \quad \boldsymbol{\Phi} = \left[\boldsymbol{\varphi}_1 \quad \cdots \quad \boldsymbol{\varphi}_m \right] \right\} \tag{5}$$

The global mode shape $\boldsymbol{\varphi}_i$ is assumed to be normalised to unity throughout this work, i.e., $\boldsymbol{\varphi}_i^T \boldsymbol{\varphi}_i = 1 \left(i = 1, \cdots, m \right)$, to make the model identifiable.

Let $\mathcal{D} = \left\{ \left\{ \hat{\mathcal{F}}_k^{(1)} \right\}, \cdots, \left\{ \hat{\mathcal{F}}_k^{(n_s)} \right\} \right\}$ denote the collection of the FFTs within the selected band in all setups. Using Bayes' theorem and assuming a uniform prior distribution for $\boldsymbol{\theta}$, the posterior PDF is proportional to the likelihood function, i.e., $p\left(\boldsymbol{\theta} \middle| \mathcal{D} \right) \propto p\left(\mathcal{D} \middle| \boldsymbol{\theta} \right)$. Assuming that for given $\boldsymbol{\theta}$ the modal forces and prediction errors in different setups are independent, this implies that the scaled FFT of the data in different setups are also independent. Consequently,

$$p\left(\mathcal{D} \middle| \boldsymbol{\theta} \right) = \prod_{r=1}^{n_s} p\left(\left\{ \hat{\mathcal{F}}_k^{(r)} \right\} \middle| \boldsymbol{\theta} \right) \tag{6}$$

For long data, the FFTs $\left\{ \hat{\mathcal{F}}_k^{(r)} \right\}$ follow a (circular symmetric) complex Gaussian distribution and are independent at different frequencies [1], giving

$$p\left(\left\{ \hat{\mathcal{F}}_k^{(r)} \right\} \middle| \boldsymbol{\theta} \right) = \prod_k \frac{\pi^{-n_r}}{\left| \mathbf{E}_k^{(r)} \left(\boldsymbol{\theta} \right) \right|} \exp\left[-\hat{\mathcal{F}}_k^{(r)*} \mathbf{E}_k^{(r)} \left(\boldsymbol{\theta} \right)^{-1} \hat{\mathcal{F}}_k^{(r)} \right] \tag{7}$$

where the product is taken over all the frequencies within the selected band; $\mathbf{E}_k^{(r)}$ is the theoretical PSD matrix of the data in Setup *r*; assuming that the prediction errors $\boldsymbol{\varepsilon}_k^{(r)}$ are independent of the modal forces $\mathbf{p}_k^{(r)}$, it is given by

$$\mathbf{E}_k^{(r)} = E\left[\hat{\mathcal{F}}_k^{(r)} \hat{\mathcal{F}}_k^{(r)*} \middle| \boldsymbol{\theta} \right] = \boldsymbol{\Phi}_r \mathbf{H}_k^{(r)} \boldsymbol{\Phi}_r^T + S_e^{(r)} \mathbf{I}_{n_r} \tag{8}$$

where $\mathbf{H}_k^{(r)} = \mathbf{h}_k^{(r)} \mathbf{S}^{(r)} \mathbf{h}_k^{(r)*}$ and '*' denotes the complex conjugate transpose.

In implementation, it is more convenient to work with the log-likelihood function (LLF) for computation and analysis:

$$L\left(\boldsymbol{\theta} \right) = \ln p\left(\mathcal{D} \middle| \boldsymbol{\theta} \right) = \sum_{r=1}^{n_s} L_r \tag{9}$$

where

$$L_r = -n_r N_f^{(r)} \ln \pi - \sum_k \ln \left| \mathbf{E}_k^{(r)} \right| - \sum_k \hat{\mathcal{F}}_k^{(r)*} \mathbf{E}_k^{(r)-1} \hat{\mathcal{F}}_k^{(r)} \tag{10}$$

and the sums are over all frequencies in the selected band; $N_f^{(r)}$ is the number of FFT points in the selected band of Setup *r*. Note that in the BAYOMA literature $L(\boldsymbol{\theta})$ refers to the negative LLF but here it refers directly to the LLF. This is to be consistent with the EM literature.

The MPV of modal parameters $\boldsymbol{\theta}$ (akin to the 'best' estimate in non-Bayesian methods) can be determined by maximising $L(\boldsymbol{\theta})$ in (9) (equivalent to maximising $p(\boldsymbol{\theta}|\mathcal{D})$). It involves repeated calculation of the determinant and inverse of $\mathbf{E}_k^{(r)}$ at different *k* and different trial values of $\boldsymbol{\theta}$. The computation is non-trivial since the matrix $\mathbf{E}_k^{(r)}$ is close to being singular especially for good quality data with high s/n ratio. On the other hand, the dimension of $\mathbf{E}_k^{(r)}$, which is equal to the number of measured DOFs, could be large in applications. The aforementioned difficulties render direct calculation based on the original formulation impractical in implementation. An efficient algorithm [25] has been developed for well-separated modes (i.e., $m = 1$) in multiple setup OMA, allowing one to compute the modal properties within several seconds, even for a large number of DOFs. That algorithm, however, cannot be easily extended to deal with close modes (i.e., more than one mode in the selected band) because the measured mode shapes are not necessarily orthogonal and the modal excitations could be correlated and hence have a non-zero coherence (correlation in the frequency domain). A method has been recently developed based on EM to improve the computational efficiency and robustness in the case of single setup [34]. It allows the parameters other than natural frequencies and damping ratios to be updated analytically in terms of the remaining parameters, which significantly reduces the number of parameters to be numerically optimised. In the case of multiple setup OMA that is considered in this work, as detailed in Section 4, it is still feasible to update analytically the MPVs of some parameters given the remaining ones based on EM algorithm, thereby providing an efficient semi-analytical iterative algorithm for modal identification.

3. Expectation-Maximisation algorithm

Before employing the EM algorithm to Bayesian FFT method in multiple setup problem, we first briefly introduce this algorithm and its variant which will be used in the paper. A thorough review of the theory and applications of this algorithm can be found in [36]. The EM algorithm

is widely used to determine the maximum likelihood estimates of the parameters $\boldsymbol{\theta}$ in a statistical model $p\left(\mathbf{Y}|\boldsymbol{\theta}\right)$ where $\mathbf{Y}$ is the observed data. By introducing a 'latent variable' $\mathbf{X}$ (which must be carefully designed), it provides the opportunity for exploiting the mathematical structure of the subject problem to produce an algorithm where different groups of parameters are updated iteratively and where the LLF is guaranteed to increase (hence closer to solution). In the context of Bayesian modal identification, $\boldsymbol{\theta}$ is the set of modal parameters to be identified (i.e., (5)) while $\mathbf{Y}$ is the data FFTs $\mathcal{D}$. Following the findings in [34], the modal response $\left\{\boldsymbol{\eta}_k^{(r)}\right\}$ is taken as the latent variable in this work, which is found to result in an efficient algorithm. The EM algorithm seeks to find the maximum likelihood estimates by alternating between performing the Expectation (E) step and the Maximisation (M) step until convergence:

E step: The expected value of the 'complete-data log likelihood' $L\left(\boldsymbol{\theta};\mathbf{Y},\mathbf{X}\right)=\ln p\left(\left\{\mathbf{Y},\mathbf{X}\right\}|\boldsymbol{\theta}\right)$ is computed, i.e.,

$$Q\left(\boldsymbol{\theta}\middle|\boldsymbol{\theta}^{(t)}\right)=\mathrm{E}_{\mathbf{X}|\mathbf{Y},\boldsymbol{\theta}^{(t)}}\left[L\left(\boldsymbol{\theta};\mathbf{Y},\mathbf{X}\right)\right] \tag{11}$$

where $\mathrm{E}_{\mathbf{X}|\mathbf{Y},\boldsymbol{\theta}^{(t)}}\left[\bullet\right]$ is the expectation operation with respect to the current conditional distribution of $\mathbf{X}$ given $\mathbf{Y}$ and the current estimates of parameters $\boldsymbol{\theta}^{(t)}$.

M step: Update the parameters by maximising (11), i.e.,

$$\boldsymbol{\theta}^{(t+1)}=\arg\max_{\boldsymbol{\theta}} Q\left(\boldsymbol{\theta}\middle|\boldsymbol{\theta}^{(t)}\right) \tag{12}$$

The EM algorithm is especially useful when the likelihood function belongs to the exponential family (as in modal identification) since the E step leads to a sum of expectation of sufficient statistics while the M step involves maximising a linear function of unknown parameters. In this case, a closed-form update for each step is usually available. The EM iterations always increase the likelihood function and therefore converge if the likelihood is bounded [37]. There is no guarantee that the sequence converges to a global maximum, however. Depending on the initial value of $\boldsymbol{\theta}$, EM may converge to a saddle point or a local maximum. To avoid such an issue, a proper initial guess of $\boldsymbol{\theta}$ should be provided when using the EM algorithm.

One drawback of EM is the possibility of low convergence which is problem dependent and does not reveal itself in a trivial manner. In particular, it can happen for some problems that

the iterations move quickly to the neighbourhood of a stationary point but then move extremely slow (or practically stagnant) towards the stationary point. Different variants have been proposed for improvement, among which the P-EM [38,39] shows good efficiency while still preserving the advantages of the EM algorithm, i.e., simplicity and monotonic convergence. The P-EM approximates the local curvature of the surface ($\boldsymbol{\theta}$, $L(\boldsymbol{\theta})$) by a parabolic extrapolation controlled by three successively estimated values of parameter $\boldsymbol{\theta}$, where $L\left(\boldsymbol{\theta}\right) = \ln p\left(\mathbf{Y}\middle|\boldsymbol{\theta}\right)$. Let $F:\boldsymbol{\theta}\mapsto F\left(\boldsymbol{\theta}\right)$ be a mapping function representing a single iteration of EM so that a sequence $\boldsymbol{\theta}^{(0)}$, $\boldsymbol{\theta}^{(1)}$, …, $\boldsymbol{\theta}^{(t)}$, … can be generated with the iterative scheme, i.e., $\boldsymbol{\theta}^{(t+1)} = F\left(\boldsymbol{\theta}^{(t)}\right)$.

The pseudo-code of P-EM is given in Algorithm 1 [38].To start the algorithm, several iterations of EM need to be performed first from the initial value of $\boldsymbol{\theta}^{(0)}$. Besides, two parameters *a* and *b* need to be tuned in the extrapolation step. Good reference values are given in [38] with *a* = 1.5 and *b* = 0.1. They are used in this work.

Algorithm 1 (Pseudo-code of P-EM)

1. Initialisation

   Generate a sequence of $\boldsymbol{\theta}^{(1)}$, $\boldsymbol{\theta}^{(2)}$, …, $\boldsymbol{\theta}^{(n_b)}$ based on $\boldsymbol{\theta}^{(t+1)} = F\left(\boldsymbol{\theta}^{(t)}\right)$ from the initial value $\boldsymbol{\theta}^{(0)}$ and set $\tilde{\boldsymbol{\theta}}^{(0)} = \boldsymbol{\theta}^{(n_b)}$.

2. Iterations

   iter = 0; $L_{old} = L\left(\tilde{\boldsymbol{\theta}}^{(0)}\right)$; $\tilde{\boldsymbol{\theta}}^{(1)} = F\left(\tilde{\boldsymbol{\theta}}^{(0)}\right)$; $\tilde{\boldsymbol{\theta}}^{(2)} = F\left(\tilde{\boldsymbol{\theta}}^{(1)}\right)$; $L_{best} = L\left(\tilde{\boldsymbol{\theta}}^{(2)}\right)$

   while *iter* < *itermax* % maximum number of iterations

   iter = *iter* +1; *i* = 0; $c = 1 + a^i b$;

   $\tilde{\boldsymbol{\theta}}_{new} = \left(1-c\right)^2 \tilde{\boldsymbol{\theta}}^{(0)} + 2c\left(1-c\right)\tilde{\boldsymbol{\theta}}^{(1)} + c^2\tilde{\boldsymbol{\theta}}^{(2)}$; $L_{new} = L\left(\tilde{\boldsymbol{\theta}}_{new}\right)$;

   if $L_{new} \le L_{best}$

   $\tilde{\boldsymbol{\theta}}^{(0)} = \tilde{\boldsymbol{\theta}}^{(2)}$; $L_{old} = L_{best}$

   $\tilde{\boldsymbol{\theta}}^{(1)} = F\left(\tilde{\boldsymbol{\theta}}^{(0)}\right)$; $\tilde{\boldsymbol{\theta}}^{(2)} = F\left(\tilde{\boldsymbol{\theta}}^{(1)}\right)$; $L_{best} = L\left(\tilde{\boldsymbol{\theta}}^{(2)}\right)$

   else

   $L_{old} = L_{best}$;

   while $L_{new} > L_{best}$

   $\tilde{\boldsymbol{\theta}}_{best} = \tilde{\boldsymbol{\theta}}_{new}$; $L_{best} = L_{new}$; *i* = *i* + 1; $c = 1 + a^i b$;

   $\tilde{\boldsymbol{\theta}}_{new} = \left(1-c\right)^2 \tilde{\boldsymbol{\theta}}^{(0)} + 2c\left(1-c\right)\tilde{\boldsymbol{\theta}}^{(1)} + c^2\tilde{\boldsymbol{\theta}}^{(2)}$; $L_{new} = L\left(\tilde{\boldsymbol{\theta}}_{new}\right)$

   endwhile

$\tilde{\boldsymbol{\theta}}^{(0)} = \tilde{\boldsymbol{\theta}}^{(1)}; \tilde{\boldsymbol{\theta}}^{(1)} = \tilde{\boldsymbol{\theta}}^{(2)};\ \tilde{\boldsymbol{\theta}}^{(2)} = F\left(F\left(\tilde{\boldsymbol{\theta}}_{best}\right)\right);\ L_{best} = L\left(\tilde{\boldsymbol{\theta}}^{(2)}\right)$

endif

if $\left|L_{best} - L_{old}\right| / L_{best} < \varepsilon$ % convergence criterion

stop; % convergence achieved

endif

endwhile

4. EM for Bayesian FFT method in multiple setup data

The last section provides the recipe for EM algorithm in a general context but its feasible implementation is far from trivial. The feasibility and resulting efficiency gain depend critically on the discovery of special mathematical structure of the problem (if any) and proper design of latent variables. In the current context of Bayesian modal identification, one main issue is to determine the mapping function *F*. It involves determining (preferably analytically) the *Q*-function (i.e., expectation of complete-data log likelihood) in the E step (see (11)) and maximising it (preferably analytically) in the M step. It turns out that by defining the modal response as the latent variable these can be performed almost analytically, leading to an efficient algorithm that is also elegant and conducive to computer coding. The *Q*-function is investigated in Section 4.1. The maximisation step is solved analytically in Section 4.2, leading to closed-form expressions for updating the parameters. Section 4.3 develops the proper initial guess of modal parameters based on high modal s/n asymptotics, which is indispensable for proper convergence and robustness of the resulting algorithm.

4.1. Formulation of *Q*-function

The choice of latent variable is critical to an EM algorithm as it determines the resulting mathematical structure of the problem. In the case of data from a single setup, taking the modal response as latent variable was found to simplify complications arising from multiple modes and as a result lead to an efficient algorithm [34]. Such simplification still applies to the present context of multiple setup data, and so the modal response $\boldsymbol{\eta}_k^{(r)}$ is taken as the latent variable.

Recall that the scaled FFT at frequency $\mathrm{f}_k^{(r)} = k/N_r\Delta t_r\ (\mathrm{Hz})$ in Setup r is modelled as $\hat{\mathcal{F}}_k^{(r)} = \boldsymbol{\Phi}_r\boldsymbol{\eta}_k^{(r)} + \boldsymbol{\varepsilon}_k^{(r)}$ where $\boldsymbol{\Phi}_r = \mathbf{L}_r\boldsymbol{\Phi}$ and $\boldsymbol{\eta}_k^{(r)} = \mathbf{h}_k^{(r)}\mathbf{p}_k^{(r)}$. To formulate the *Q*-function in (11), we need to determine the complete-data log likelihood function and the conditional distribution

of $\left\{\boldsymbol{\eta}_k^{(r)}\right\}$ given $\mathcal{D}$ and $\boldsymbol{\theta}$. Since $\mathbf{p}_k^{(r)} \sim CN\left(\mathbf{0}, \mathbf{S}^{(r)}\right)$, $\boldsymbol{\eta}_k^{(r)}$ also follows a (circular symmetric) complex Gaussian distribution with a covariance of $\mathbf{H}_k^{(r)} = \mathbf{h}_k^{(r)} \mathbf{S}^{(r)} \mathbf{h}_k^{(r)*}$. Combining with $\boldsymbol{\varepsilon}_k^{(r)} \sim CN\left(0, S_e^{(r)} \mathbf{I}_{n_r}\right)$, the conditional joint distribution of $\hat{\mathcal{F}}_k^{(r)}$ and $\boldsymbol{\eta}_k^{(r)}$ given $\boldsymbol{\theta}$ is again a (circular symmetric) complex Gaussian with the covariance matrix

$$\mathbf{C}_k^{(r)} = \begin{bmatrix} \boldsymbol{\Phi}_r \mathbf{H}_k^{(r)} \boldsymbol{\Phi}_r^T + S_e^{(r)} \mathbf{I}_{n_r} & \boldsymbol{\Phi}_r \mathbf{H}_k^{(r)} \\ \mathbf{H}_k^{(r)} \boldsymbol{\Phi}_r^T & \mathbf{H}_k^{(r)} \end{bmatrix} \tag{13}$$

Using this information and by conditioning on the modal response, the complete-data log likelihood function can be expressed in an elegant form (see Appendix A for details)

$$L\left(\boldsymbol{\theta}; \left\{\hat{\mathcal{F}}_k^{(r)}, \boldsymbol{\eta}_k^{(r)}\right\}\right) = \ln p\left(\left\{\hat{\mathcal{F}}_k^{(r)}, \boldsymbol{\eta}_k^{(r)}\right\} \middle| \boldsymbol{\theta}\right) = \sum_{r=1}^{n_s} L_r \tag{14}$$

where

$$\begin{aligned} L_r = & -\left(n_r + m\right) N_f^{(r)} \ln \pi - n_r N_f^{(r)} \ln S_e^{(r)} - S_e^{(r)-1} \sum_k \left[\hat{\mathcal{F}}_k^{(r)} - \boldsymbol{\Phi}_r \boldsymbol{\eta}_k^{(r)}\right]^* \left[\hat{\mathcal{F}}_k^{(r)} - \boldsymbol{\Phi}_r \boldsymbol{\eta}_k^{(r)}\right] \\ & + \sum_k \ln \left|\mathbf{H}_k^{(r)-1}\right| - \sum_k \boldsymbol{\eta}_k^{(r)*} \mathbf{H}_k^{(r)-1} \boldsymbol{\eta}_k^{(r)} \end{aligned} \tag{15}$$

On the other hand, using (13) and standard results in multi-variate Gaussian statistics [40], the conditional distribution of $\boldsymbol{\eta}_k^{(r)}$ given $\hat{\mathcal{F}}_k^{(r)}$ and $\boldsymbol{\theta}$ is a complex Gaussian with mean

$$E\left[\boldsymbol{\eta}_k^{(r)} \middle| \hat{\mathcal{F}}_k^{(r)}, \boldsymbol{\theta}\right] = (\mathbf{J}_k^{(r)})^{-1} \boldsymbol{\Phi}_r{}^T \hat{\mathcal{F}}_k^{(r)} \tag{16}$$

and covariance

$$\mathbf{C}\left[\boldsymbol{\eta}_k^{(r)} \middle| \hat{\mathcal{F}}_k^{(r)}, \boldsymbol{\theta}\right] = S_e^{(r)} (\mathbf{J}_k^{(r)})^{-1} \tag{17}$$

where $\mathbf{J}_k^{(r)} = S_e^{(r)} \left(\mathbf{H}_k^{(r)}\right)^{-1} + \boldsymbol{\Phi}_r^T \boldsymbol{\Phi}_r$.

Taking expectation on (14) with respect to the conditional distribution of $\boldsymbol{\eta}_k^{(r)}$ given $\hat{\mathcal{F}}_k^{(r)}$ and $\boldsymbol{\theta}$ yields *Q*-function

$$Q\left(\boldsymbol{\theta} \middle| \boldsymbol{\theta}^{(t)}\right) = \sum_{r=1}^{n_s} \left\{-\left(n_r + m\right) N_f^{(r)} \ln \pi - n_r N_f^{(r)} \ln S_e^{(r)} - S_e^{(r)-1} Q_1^{(r)}\left(\boldsymbol{\theta} \middle| \boldsymbol{\theta}^{(t)}\right) + Q_2^{(r)}\left(\boldsymbol{\theta} \middle| \boldsymbol{\theta}^{(t)}\right)\right\} \tag{18}$$

where

$$Q_1^{(r)}\left(\boldsymbol{\theta}\middle|\boldsymbol{\theta}^{(t)}\right)=\sum_k\left\{\hat{\mathcal{F}}_k^{(r)*}\hat{\mathcal{F}}_k^{(r)}-2tr\left[\boldsymbol{\Phi}_r\,\mathrm{Re}\left(\mathbf{w}_{1k}^{(r)}\hat{\mathcal{F}}_k^{(r)*}\right)\right]+tr\left[\boldsymbol{\Phi}_r\mathbf{w}_{2k}^{(r)}\boldsymbol{\Phi}_r^T\right]\right\} \tag{19}$$

$$Q_2^{(r)}\left(\boldsymbol{\theta}\middle|\boldsymbol{\theta}^{(t)}\right)=\sum_k\ln\left|\mathbf{H}_k^{(r)-1}\right|-tr\left(\sum_k\mathbf{H}_k^{(r)-1}\mathbf{w}_{2k}^{(r)}\right) \tag{20}$$

The terms $\mathbf{w}_{1k}^{(r)}=E_{\boldsymbol{\eta}_k^{(r)}\left|\hat{\mathcal{F}}_k^{(r)},\boldsymbol{\theta}^{(t)}\right.}\left[\boldsymbol{\eta}_k^{(r)}\right]$ and $\mathbf{w}_{2k}^{(r)}=E_{\boldsymbol{\eta}_k^{(r)}\left|\hat{\mathcal{F}}_k^{(r)},\boldsymbol{\theta}^{(t)}\right.}\left[\boldsymbol{\eta}_k^{(r)}\boldsymbol{\eta}_k^{(r)*}\right]$ are respectively the first and second conditional moment of $\boldsymbol{\eta}_k^{(r)}$ given $\hat{\mathcal{F}}_k^{(r)}$ and $\boldsymbol{\theta}^{(t)}$ (parameters obtained from previous iteration). The former can be calculated using (16) and the latter using

$$\mathbf{w}_{2k}^{(r)}=(\mathbf{J}_k^{(r)})^{-1}\boldsymbol{\Phi}_r{}^T\hat{\mathcal{F}}_k^{(r)}\hat{\mathcal{F}}_k^{(r)*}\boldsymbol{\Phi}_r(\mathbf{J}_k^{(r)})^{-*}+S_e^{(r)}(\mathbf{J}_k^{(r)})^{-1} \tag{21}$$

Note that $\mathbf{w}_{1k}^{(r)}$ and $\mathbf{w}_{2k}^{(r)}$ are constant in the M-step since they are evaluated based on the parameters obtained in the previous iteration. Equation (18) indicates that the mode shape affects the *Q*-function solely through the third term while the forth term involves the modal parameters other than $S_e^{(r)}$ and $\boldsymbol{\Phi}_r$. Consequently, the parameters can be optimised in different groups in the M-step.

4.2. Maximisation of *Q*-function

In the M-step, the parameters are updated by maximising $Q\left(\boldsymbol{\theta}\middle|\boldsymbol{\theta}^{(t)}\right)$ with respect to $\boldsymbol{\theta}$. By exploiting the mathematical structure of the Q-function in (18), analytical closed-form solution can be obtained for the modal force PSDs, noise PSDs and mode shapes. First consider the (global) mode shape $\boldsymbol{\Phi}(n\times m)$ which is related to the local mode shape matrix by $\boldsymbol{\Phi}_r=\mathbf{L}_r\boldsymbol{\Phi}$ $(n_r\times m)$. By noting that in (18) only Q_1 depends on $\boldsymbol{\Phi}$, one obtains

$$\frac{\partial Q\left(\boldsymbol{\theta}\middle|\boldsymbol{\theta}^{(t)}\right)}{\partial\boldsymbol{\Phi}}=\sum_{r=1}^{n_s}\left\{2S_e^{(r)-1}\sum_k\mathrm{Re}\left(\mathbf{L}_r^T\mathcal{F}_k^{(r)}\mathbf{w}_{1k}^{(r)*}\right)-2S_e^{(r)-1}\mathbf{L}_r^T\mathbf{L}_r\boldsymbol{\Phi}\sum_k\mathrm{Re}\left(\mathbf{w}_{2k}^{(r)}\right)\right\} \tag{22}$$

where we have used $d\left\{tr\left(\mathbf{UXV}\right)\right\}/d\mathbf{X}=\mathbf{U}^T\mathbf{V}^T$ and $d\left\{tr\left(\mathbf{UXCX}^T\mathbf{V}\right)\right\}/d\mathbf{X}=\mathbf{U}^T\mathbf{V}^T\mathbf{XC}^T+\mathbf{VUXC}$ for any matrices **U**, **X**, **C** and **V** of appropriate size with **U**, **C** and **V** being constant. For simplicity, define

$$\mathbf{A}_r = S_e^{(r)-1}\mathbf{L}_r^T\mathbf{L}_r \in R^{n\times n} \quad \mathbf{B}_r = \sum_k \mathrm{Re}\left(\mathbf{w}_{2k}^{(r)}\right) \in R^{m\times m} \quad \mathbf{P} = \sum_{r=1}^{n_s}\left\{ S_e^{(r)-1}\sum_k \mathrm{Re}\left[\mathbf{L}_r^T \mathbf{F}_k^{(r)} \mathbf{w}_{1k}^{(r)*}\right]\right\} \in R^{n\times m} \quad (23)$$

Note that $\mathbf{A}_r$ is a diagonal matrix and its *i*-th diagonal entry is equal to the product of $S_e^{(r)-1}$ and the number of channels DOF *i* is measured in setup *r*. To see this, note that the (*i*, *j*)-entry of $\mathbf{A}_r$ is equal to $\mathbf{A}_r(i,j) = S_e^{(r)-1}\sum_{k=1}^{n_r}\mathbf{L}_r(k,i)\mathbf{L}_r(k,j)$, where $\mathbf{L}_r$ (*k*, *i*) is either 1 (when local channel *k* measures DOF *i*) or zero (otherwise). Thus when *i* = *j*, the summand $\sum_{k=1}^{n_r}\mathbf{L}_r(k,i)\mathbf{L}_r(k,j)$ simply counts the number of local channels in setup *r* that measure DOF *i*. When *i* is not equal to *j*, the summand $\sum_{k=1}^{n_r}\mathbf{L}_r(k,i)\mathbf{L}_r(k,j)$ is zero because a single channel *k* cannot measure both DOFs *i* and *j* (assumed to be distinct).

The term $\mathbf{B}_r$ is a constant matrix in the current step because it is evaluated based on the parameters from the previous iteration. Setting the derivative in (22) to zero and rearranging, one obtains the equation:

$$\left[\sum_{r=1}^{n_s}\left(\mathbf{A}_r \otimes \mathbf{B}_r^T\right)\right] vec(\mathbf{\Phi}^T) = vec(\mathbf{P}^T) \quad (24)$$

where ' $\otimes$ ' denotes the Kronecker product; $vec(\bullet)$ denotes the vectorisation of the corresponding matrix, obtained by stacking its columns. Note that the Kronecker product $\mathbf{A}_r \otimes \mathbf{B}_r^T$ gives a diagonal block matrix because $\mathbf{A}_r$ is diagonal. The summation in the bracket of (24) is invertible because $\mathbf{B}_r$ is and all the DOFs considered are measured by at least one data channel (hence all the diagonal blocks are non-zero). Consequently, after rearranging, one has

$$\mathbf{\Phi}(i) = \mathbf{P}(i)\left[\sum_{r=1}^{n_s}(\mathbf{A}_r(i,i)\mathbf{B}_r)\right]^{-1}, i = 1,\cdots,n \quad (25)$$

where $\mathbf{\Phi}(i)$ and $\mathbf{P}(i)$ are respectively the *i*-th row of $\mathbf{\Phi}$ and $\mathbf{P}$. The term to be taken inverse in the bracket is a *m*-by-*m* matrix where *m* typically does not exceed 3; the computational time involved is therefore negligible. It should be noted that the mode shape norm constraints have been ignored when deriving (25) and they can be handled by simply scaling the mode shapes

in (25) to have unit norm (see later). Such strategy has been proved to be legitimate for EM algorithm [34].

We next consider the update of noise PSDs and modal force PSDs. Taking the partial derivative of $Q\left(\boldsymbol{\theta}\middle|\boldsymbol{\theta}^{(t)}\right)$ in (18) with respect to $S_e^{(r)-1}$ and setting it to zero gives

$$S_e^{(r)} = \frac{Q_1^{(r)}\left(\boldsymbol{\theta}\middle|\boldsymbol{\theta}^{(t)}\right)}{n_r N_f^{(r)}} \tag{26}$$

Similarly, it is shown in Appendix A that the update of $\mathbf{S}^{(r)}$ is given by

$$\mathbf{S}^{(r)} = \frac{1}{N_f^{(r)}} \sum_k \left(\mathbf{h}_k^{(r)-1} \mathbf{w}_{2k}^{(r)} \mathbf{h}_k^{(r)-*}\right) \tag{27}$$

Closed-form expressions are not available for natural frequencies $\left\{f_i^{(r)}\right\}$ and damping ratios $\left\{\zeta_i^{(r)}\right\}$ because they affect the *Q*-function in a nonlinear manner that is not amendable to analytical treatment. As shown in Appendix B, the gradient and Hessian of the *Q*-function can be derived analytically with respect to these parameters. Newton's method is therefore used for efficiently optimising $\left\{f_i^{(r)}\right\}$ and $\left\{\zeta_i^{(r)}\right\}$ given the remaining parameters. Since the optimisation of $\left\{f_i^{(r)}\right\}$ and $\left\{\zeta_i^{(r)}\right\}$ is coupled in a top-level iteration, it is generally sufficient to determine them as a solution using a single Newton iteration in each M-step. This improves the efficiency of the algorithm but without introducing any approximation in the final (top-level) converged solution because the remaining parameters are continually updated through the top-level iteration.

As mentioned earlier mode shape constraints can be incorporated by simply scaling each mode shape in (25) to have unit norm, i.e.,

$$\hat{\boldsymbol{\Phi}} = \boldsymbol{\Phi}\mathbf{a} \tag{28}$$

where $\hat{\boldsymbol{\Phi}}$ is the MPV of mode shape; $\mathbf{a}$ is a *m*-by-*m* diagonal matrix with the *i*-th diagonal entry being $1/\|\boldsymbol{\varphi}_i\|$. Correspondingly, the modal force PSD $\mathbf{S}^{(r)}$ updated in the M-step should be scaled as

$$\hat{\mathbf{S}}^{(r)} = \mathbf{a}^{-1}\mathbf{S}^{(r)}\mathbf{a}^{-1} \tag{29}$$

It can be easily checked that the theoretical PSD matrix based on the mode shapes in (28) and modal force PSD matrix in (29) is invariant to the scaling, as can be intuitively expected.

4.3. Initial guess of modal parameters

A proper initial guess is important to start an iterative algorithm in a domain of convergence. In this section, we investigate the initial guess of modal parameters based on the asymptotic behaviour of their MPVs when the modal s/n ratio is high that simplifies mathematics. For this purpose, (10) is first rewritten as (see Appendix A for details)

$$\begin{aligned} L_r &= -n_r N_f^{(r)} \ln \pi - \left(n_r - m\right) N_f^{(r)} \ln S_e^{(r)} - \\ &\sum_k \ln \left|\mathbf{J}_k^{(r)}\right| - \sum_k \ln \left|\mathbf{H}_k^{(r)}\right| - S_e^{(r)-1} \left(\sum_k \mathcal{F}_k^{(r)*} \mathcal{F}_k^{(r)} - \sum_k \mathbf{s}_k^{(r)*} \mathbf{J}_k^{(r)-1} \mathbf{s}_k^{(r)} \right) \end{aligned} \tag{30}$$

where $\mathbf{s}_k^{(r)} = \boldsymbol{\Phi}_r^T \mathcal{F}_k^{(r)}$. By writing LLF in this form, the asymptotic MPVs of $S_e^{(r)}$ and $\mathbf{S}^{(r)}$ can be obtained analytically when the modal s/n ratio is high. In such a situation, $S_e^{(r)} \left(\mathbf{H}_k^{(r)}\right)^{-1} \to \mathbf{0}$, one has

$$\mathbf{J}_k^{(r)} \sim \boldsymbol{\Phi}_r^T \boldsymbol{\Phi}_r \tag{31}$$

and (up to the first order)

$$\mathbf{J}_k^{(r)-1} \sim \left(\boldsymbol{\Phi}_r^T \boldsymbol{\Phi}_r\right)^{-1} - S_e^{(r)} \left(\boldsymbol{\Phi}_r^T \boldsymbol{\Phi}_r\right)^{-1} \left(\mathbf{H}_k^{(r)}\right)^{-1} \left(\boldsymbol{\Phi}_r^T \boldsymbol{\Phi}_r\right)^{-1} \tag{32}$$

Substituting (31) and (32) into (30) gives

$$\begin{aligned} L_r &\sim -n_r N_f^{(r)} \ln \pi - \left(n_r - m\right) N_f^{(r)} \ln S_e^{(r)} - \sum_k \ln \left|\boldsymbol{\Phi}_r^T \boldsymbol{\Phi}_r\right| - \sum_k \ln \left|\mathbf{H}_k^{(r)}\right| \\ &- S_e^{(r)-1} \left(\sum_k \mathcal{F}_k^{(r)*} \mathcal{F}_k^{(r)} - \sum_k \mathbf{s}_k^{(r)*} \left[\left(\boldsymbol{\Phi}_r^T \boldsymbol{\Phi}_r\right)^{-1} - S_e^{(r)} \left(\boldsymbol{\Phi}_r^T \boldsymbol{\Phi}_r\right)^{-1} \left(\mathbf{H}_k^{(r)}\right)^{-1} \left(\boldsymbol{\Phi}_r^T \boldsymbol{\Phi}_r\right)^{-1} \right] \mathbf{s}_k^{(r)} \right) \end{aligned} \tag{33}$$

Note that the prediction error $S_e^{(r)}$ in Setup *r* is only involved in the second and last terms in (33). The MPV of $S_e^{(r)}$ can thus be determined by maximising these two terms. This yields the asymptotic MPV of $S_e^{(r)}$ (assuming $n_r > m$)

$$S_e^{(r)} \sim \frac{\sum_k \mathcal{F}_k^{(r)*} \mathcal{F}_k^{(r)} - \sum_k \mathcal{F}_k^{(r)*} \boldsymbol{\Phi}_r \left(\boldsymbol{\Phi}_r^T \boldsymbol{\Phi}_r\right)^{-1} \boldsymbol{\Phi}_r^T \mathcal{F}_k^{(r)}}{\left(n_r - m\right) N_f^{(r)}} \tag{34}$$

Similarly, as shown in Appendix A, the asymptotic MPV of $\mathbf{S}^{(r)}$ can be obtained as

$$\mathbf{S}^{(r)} \sim \frac{1}{N_f^{(r)}} \sum_k \left(\mathbf{h}_k^{(r)}\right)^{-1} \left(\mathbf{\Phi}_r^T \mathbf{\Phi}_r\right)^{-1} \mathbf{\Phi}_r^T \mathcal{F}_k^{(r)} \mathcal{F}_k^{(r)*} \mathbf{\Phi}_r \left(\mathbf{\Phi}_r^T \mathbf{\Phi}_r\right)^{-1} \left(\mathbf{h}_k^{(r)*}\right)^{-1} \tag{35}$$

The asymptotic MPVs of $S_e^{(r)}$ and $\mathbf{S}^{(r)}$ can be used as their initial guess. For natural frequencies $\left\{f_i^{(r)}\right\}$, the initial guess can be simply picked from the singular value (SV) spectrum of the measured data. A nominal value of 1% (say) may be assigned as the initial guess of damping ratios $\left\{\zeta_i^{(r)}\right\}$. For the mode shapes, we can first set the local mode shape $\mathbf{v}_{ri}$ as the eigenvector (corresponding to the largest eigenvalue) of the real part of sample PSD matrix of the data in Setup *r* at the initial guess of natural frequency. The initial guess of global mode shape can then be set from a local least squares algorithm, e.g.,[1].

In summary, based on the analysis in Section 4, we can use Algorithm 1 to determine the MPV of modal parameters incorporating the data from multiple setups. The $\mathbf{\Phi}$, $S_e^{(r)}$ and $\mathbf{S}^{(r)}$ can be updated analytically by (25), (26) and (27), respectively, followed by a normalisation in (28) and (29), respectively. Newton method is used for updating $\left\{f_i^{(r)}\right\}$ and $\left\{\zeta_i^{(r)}\right\}$. As shown in Algorithm 1, the original EM algorithm needs to run first for generating a sequence of the parameters. Here we use the convergence of $S_e^{(r)}$ to control the number of sequences n_b, because this parameter often converges more quickly compared to others.

5. Verification and applications

5.1. Shear building (synthetic data)

Consider a six-story shear building as shown in Figure 1, where the locations to be measured are indicated by dots. The structure was considered in [41] to verify an iterative algorithm for the case of multiple modes with single setup data. The floor plan measures 36.6 m × 36.6 m. The height of the first story is 5.49 m while that of all others is 3.81 m. Assuming rigid floor, the interstory stiffness and floor mass are summarised in Table 3. The natural frequencies of the first three modes are calculated to be 2.126, 2.178 and 2.472 Hz, corresponding to the fundamental translational modes along EW (*x*) and NS (*y*) directions and the fundamental rotational mode. The damping ratios of the modes in EW, NS and rotational directions are assumed to be respectively 0.5%, 1.5% and 1%. The building is subjected to i.i.d. Guassian

white noise excitation at all the floor levels, with a one-sided PSD of $0.5\mathrm{N}/\sqrt{\mathrm{Hz}}$, $1.0\,\mathrm{N}/\sqrt{\mathrm{Hz}}$ and $3\,\mathrm{N}\cdot\mathrm{m}/\sqrt{\mathrm{Hz}}$ in EW, NS and rotational directions, respectively. The measured acceleration is contaminated by measurement noise modelled by i.i.d. Guassian white noise at different channels with a PSD of $1\mu\mathrm{g}/\sqrt{\mathrm{Hz}}$. In [41] ambient data at all the 36 × 2 = 72 DOFs to be measured was assumed to be available in a single setup but here we assume that only seven biaxial accelerometers are available, using one reference sensor and six setups to cover all the DOFs. The reference location is at Test Point 18. The detailed plan is shown in Table 4. For convenience of planning, Rover 3 in Setup 1 is put at the same location as the reference. As the setups proceed, the sensors rove from the top floor to the bottom. Acceleration data in each setup is sampled at 100 Hz for a duration of 5 minutes.

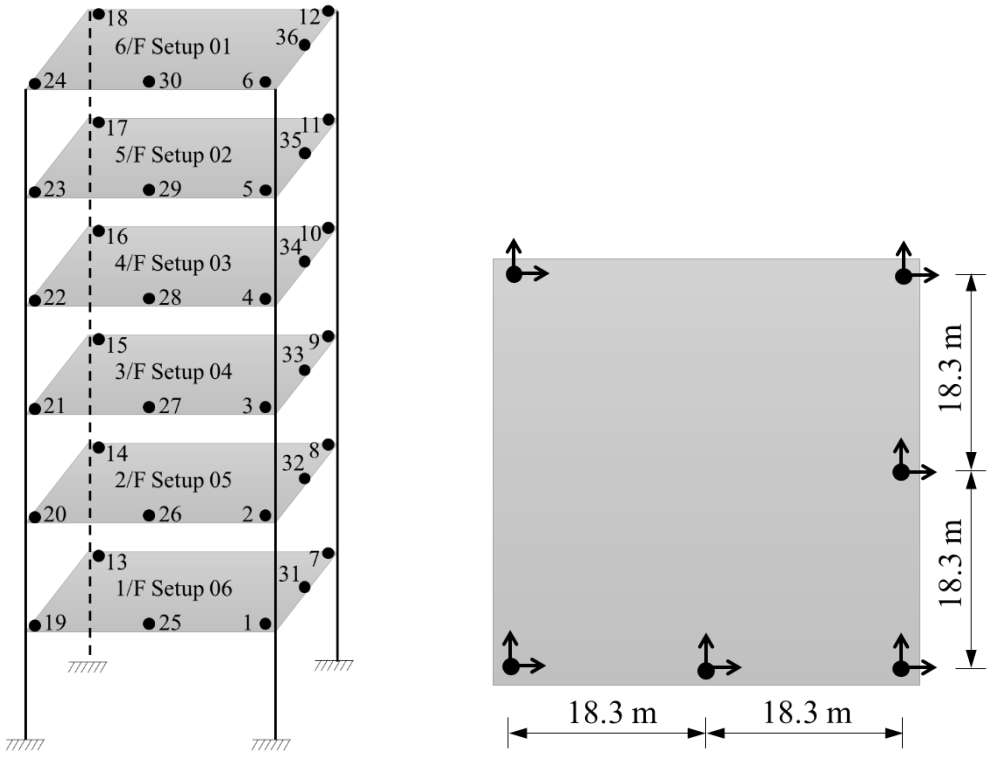

Figure 1 shear building with measured DOFs numbered and indicated by dots; Left: 3D model; Right: typical floor plan

Figure 2 (a) shows the root PSD spectrum of the data in Setup 1. Clear spectral peaks indicate the existence of structural modes. Acceleration PSD is in the order of few of $\mu\mathrm{g}/\sqrt{\mathrm{Hz}}$ around the resonance band of the modes. From the spectrum, the noise level of the data is around $1\mu\mathrm{g}/\sqrt{\mathrm{Hz}}$, which checks with the measurement noise value assumed. Figure 2 (b) shows the corresponding SV spectrum where the number of lines significantly above others indicates the number of modes. Analysis here focuses on the first six modes, which have been labelled with

their modal nature. The prefix 'TX', 'TY' and 'R' denote respectively the translational modes along *x* and *y* directions, and rotational mode. The modes TX1 and TY1 (or TX2 and TY2) are close due to the similar interstory stiffness along the two directions. To investigate the proposed method for different number of modes in the selected band, TX1, TY1 and R1 are identified in the same band (m = 3); TX2 and TY2 are identified in a single band (m = 2) while R2 is identified alone (m = 1). The (hand-picked) frequency bands and the initial guess of natural frequencies are shown with the symbol '[-]' and a circle, respectively.

Table 3 Properties of shear building

Story	Stiffness			Mass		
	x (kN/mm)	*y* (kN/mm)	Rotation (GN m/rad)	*x* (ton)	*y* (ton)	Rotation (kton m^2)
1	476	499	97.5	282	282	42.8
2	1420	1491	291	262	262	39.8
3	954	1002	196	255	255	38.7
4	954	1002	196	254	254	38.6
5	579	608	119	247	247	37.4
6	579	608	119	215	215	32.6

Table 4. Setup plan in shear building example

Setup	Sensors							Remarks
	Ref. 1	Rover 1	Rover 2	Rover 3	Rover 4	Rover 5	Rover 6	
1	18	6	12	18	24	30	36	6/F
2	18	5	11	17	23	29	35	5/F
3	18	4	10	16	22	28	34	4/F
4	18	3	9	15	21	27	33	3/F
5	18	2	8	14	20	26	32	2/F
6	18	1	7	13	19	25	31	1/F

It should be mentioned that Mode R2 can also be identified by the existing algorithm developed in [25] as it is a well-separated mode. However, this is not the case for Mode TX2 and TY2 (or TX1 and TY1), because their natural frequencies are so close that it is difficult to select a frequency band that is only dominated by one of the modes (as required by the existing algorithm).

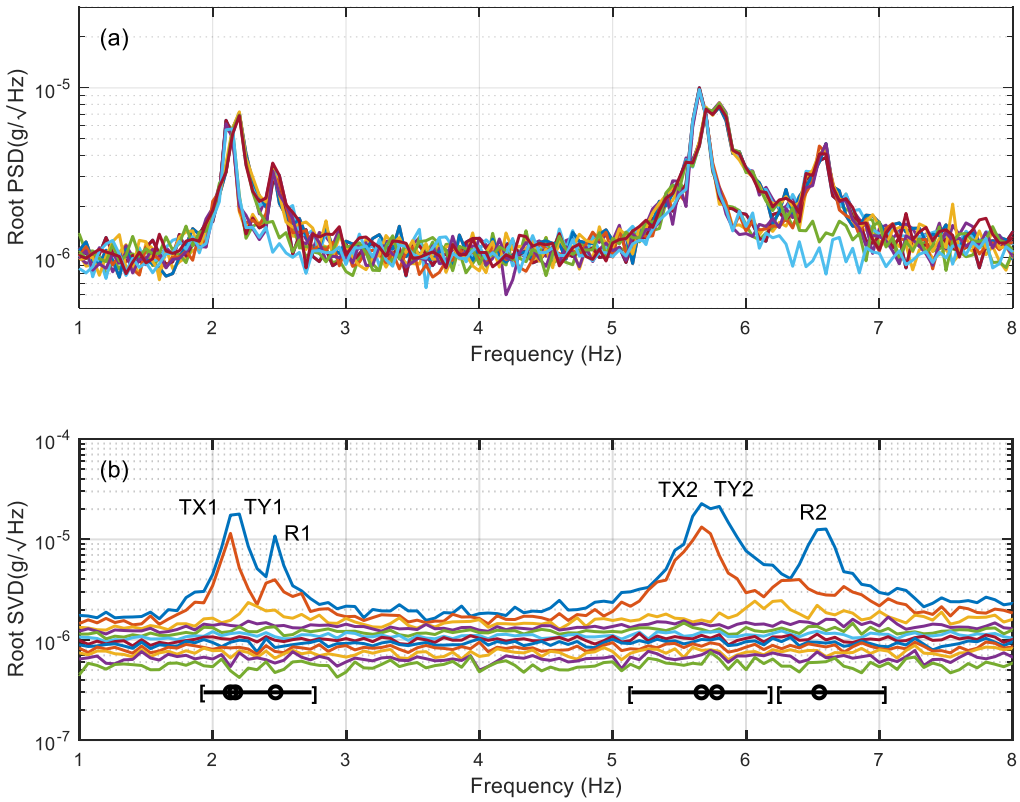

Figure 2 (a) PSD spectrum and (b) SV Spectrum. Setup 1, shear building example

Table 5 summarises the identified modal properties and the exact values used to generate the data, where S_{ii} denotes the diagonal entries of modal force PSD matrix. It is seen that the MPVs are close to the exact values. A better agreement can be achieved for the natural frequencies compared to damping ratios. This is consistent with the common observations (i.e., identified damping ratio often has a higher uncertainty). For the higher modes (say R2), the MPV of prediction error PSD tends to be larger than the exact value because of the presence of the unmodelled lower modes in the selected band. Figure 3 shows the most probable mode shapes of the first six modes of the structure where the red and black line indicates the undeformed and deformed shapes of the building, respectively. The natural frequencies and damping ratios are also reported in the figure in terms of the sample mean among the setups. The identified mode shapes are colinear with the exact ones indicated by the MACs (Modal Assurance Criterion) in Table 6.

Table 5 Identified modal parameters (MPV), shear building example

Parameter	Mode	Setup						Exact
		1	2	3	4	5	6	
f (Hz)	TX1	2.119	2.119	2.119	2.119	2.118	2.119	2.126
	TY1	2.177	2.178	2.178	2.177	2.179	2.178	2.178
	R1	2.477	2.477	2.475	2.477	2.476	2.478	2.472
	TX2	5.650	5.650	5.650	5.647	5.649	5.648	5.647
	TY2	5.768	5.773	5.767	5.768	5.768	5.769	5.786
	R2	6.563	6.559	6.558	6.559	6.562	6.561	6.566
ζ (%)	TX1	0.51	0.53	0.49	0.50	0.52	0.54	0.50
	TY1	1.37	1.25	1.17	1.32	1.28	1.15	1.50
	R1	1.13	1.02	1.05	1.09	1.05	1.18	1.00
	TX2	0.52	0.54	0.50	0.54	0.47	0.55	0.50
	TY2	1.37	1.38	1.49	1.36	1.43	1.44	1.50
	R2	0.97	0.99	1.08	1.05	0.98	0.94	1.00
$\sqrt{S_{ii}}\left(\mu g/\sqrt{Hz}\right)$	TX1	0.519	0.522	0.502	0.513	0.524	0.535	0.514
	TY1	1.034	0.986	0.952	1.018	0.993	0.941	1.028
	R1	0.471	0.456	0.462	0.470	0.457	0.485	0.480
	TX2	0.484	0.500	0.476	0.500	0.464	0.503	0.506
	TY2	0.994	0.998	1.044	0.989	1.013	1.019	1.012
	R2	0.433	0.451	0.483	0.466	0.444	0.437	0.473
$\sqrt{S_e}\left(\mu g/\sqrt{Hz}\right)$	{TX1, TY1, R1}	0.989	1.000	1.012	0.995	0.995	1.002	1.000
	{TX2, TY2}	1.052	1.033	1.025	1.020	1.044	1.031	1.000
	R2	1.314	1.139	1.090	1.154	1.194	1.196	1.000

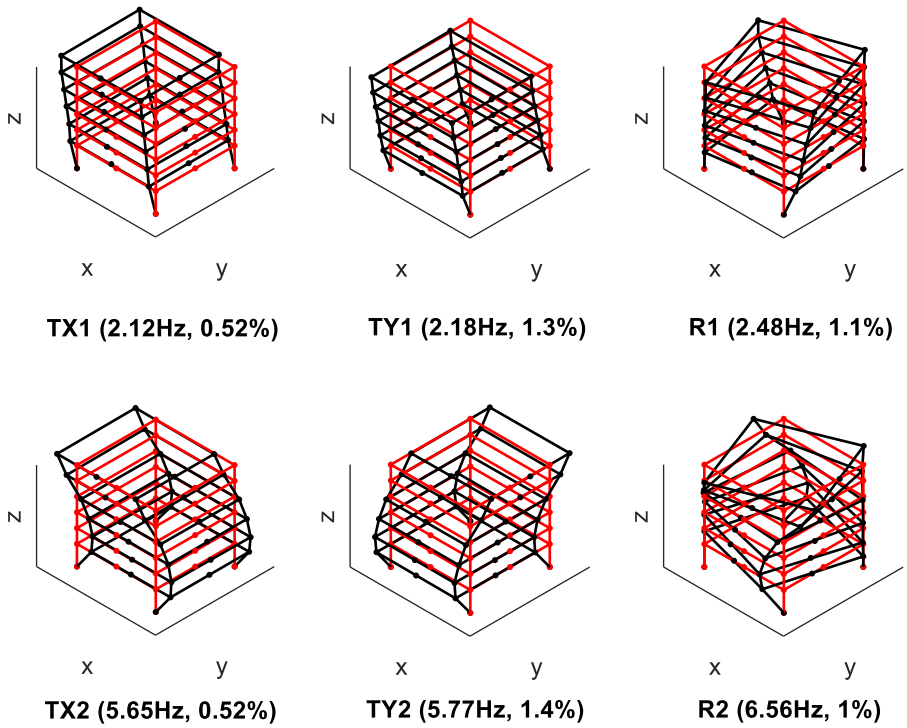

Figure 3 Identified mode shapes; shear building

Table 6 MAC between the identified and exact mode shapes

Mode	TX1	TY1	R1	TX2	TY2	R2
MAC	0.9923	0.9989	0.9980	0.9995	0.9997	0.9990

Efficient calculation of the posterior covariance matrix has not been developed in this work and so the uncertainty of modal identification results is investigated in an ensemble (frequentist) manner. For this purpose, one hundred i.i.d. data sets are generated to illustrate the statistical properties of the identified results in terms of their MPVs. Figure 4 shows the identified natural frequencies and damping ratios of the first three modes for different data durations. The results for each data length are reported with a dot at the sample mean of the MPVs and an error bar covering ±1 sample standard deviation. The dashed red line represents the exact value. As the data duration increases, the error bar shortens and the sample mean of MPV generally converges to the exact value that generated the data. The error bar covers the exact values regardless of the data durations, suggesting that the MPVs are unbiased.

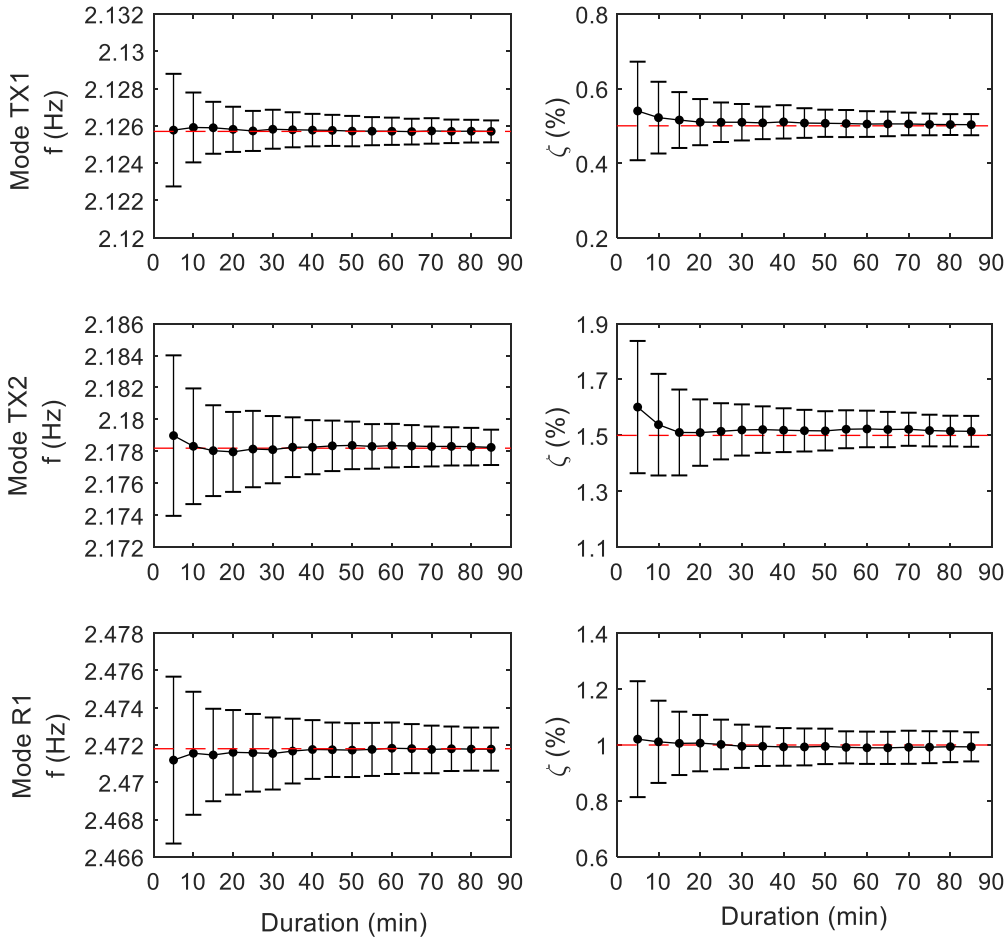

Figure 4 Identified modal properties vs duration, building example. Red dashed line – exact value; Dot: sample mean value of the MPV among 100 i.i.d. data sets; error bar: ± 1 standard deviation

From Figure 4, increasing the data duration can improve the accuracy of the estimated modal parameters, which seems to suggest one to take the measurement as long as possible in ambient vibration test. This should not be taken for granted, however, because identifying modal parameters using extended data length increases the risk of modelling error (e.g., stationary assumption of the data) in practice. The choice of the data duration is a trade-off between the amount of information for inference and the risk of modelling error. The recently developed 'uncertainty laws' for Bayesian OMA offer a fundamental means to determine the data duration for achieving a required precision of modal parameters for well-separated modes [42] and close modes [43].

5.2. Queen's park suspension footbridge (field data)

The proposed method is next applied to field data. The instrumented structure is Queen's park footbridge across the River Dee in Chester, UK (Figure 5(a)). It has a width of 4.4 m and a

main span of 85.2 m with side spans of 17.8 m each. The main deck is held up by vertical suspender cables while the side decks are supported on two piers spaced at 6 m apart. There are handrails distributed uniformly along the two sides of the bridge, providing a convenient means for locating test points. Neighbouring test points are designed to space at every two handrails. Figure 5(b) shows the plan view of the bridge and the measurement locations.

Six force-balance triaxial accelerometers were deployed in the test. Each was paired with a 24bit digitiser and logging system capable of storing data locally in a distributed manner. The recorded data of different sensors were synchronised by external GPS clocks, see Figure 6(a) for the equipment at a typical measurement point. Before the test, the instrument noise was estimated by a huddle test [44] in the laboratory with the noise spectrum of one data channel shown in Figure 6(b). It is seen that the noise level is in the order of $0.1\mu g/\sqrt{HZ}$, which is well below the ambient vibration level. Sixteen setups were designed to cover 66 locations. Details are shown in Table 7. The two reference locations, 110 and 219, were selected near the quarter and middle of the main span. The main span was measured first with two sensors roving from the west side towards the midspan and the other two roving sensors moving from the middle to the east side. Fifteen minutes data was collected at a sampling rate of 200 Hz in each setup and used for analysis. Between the setups, it generally took five minutes to move, align and level the sensors. Including initial preparation (e.g., sensor calibrations and marking test points), the whole test took around one day, from 8 am to 5 pm.

(a) Overall view of Queen's park footbridge

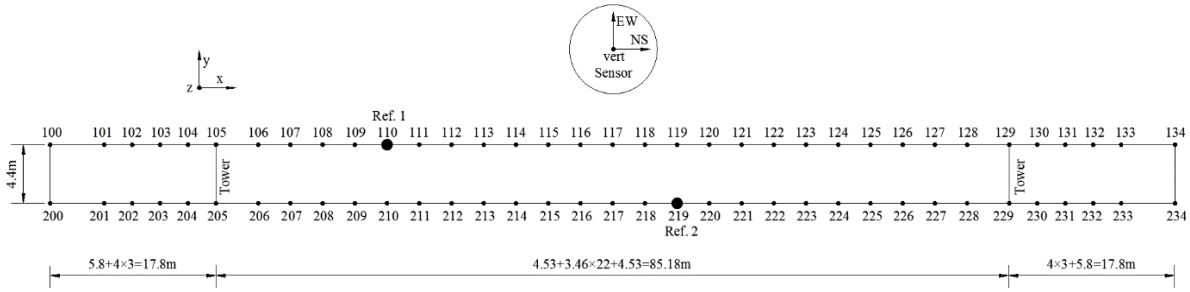

(b) Plan view and measurement locations

Figure 5 Queen's park footbridge

(a) Equipment at the test point

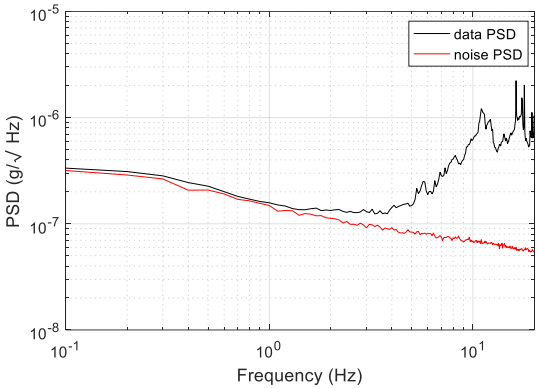

(b) Noise PSD spectrum of a typical channel

Figure 6 Equipment used in the test and its noise PSD spectrum

Figure 7 shows the SV spectrum of the data in Setup 1. It is used to select the initial guess of natural frequencies and frequency bands for modal identification, as indicated by a circle and a horizontal bar '[-]', respectively. The study here focuses on the modes below 3.5 Hz. Six modes are identified and they are named based on their nature confined from the identification results (see later). The modes are identified in group as follows: {L1}, {V1}, {V2}, {T1} and {T2, V3}. That is, the first four modes are identified separately within their bands; T2 and V3 are identified together on a single band.

Table 7 Setup Plan

Setup	Sensors						Remarks
	Ref. 1	Ref. 2	Rover 1	Rover 2	Rover 3	Rover 4	
1	110	219	205	118	217	105	Midspan
2	110	219	206	119	218	106	
3	110	219	207	120	220	107	
4	110	219	208	121	221	108	
5	110	219	209	122	222	109	
6	110	219	210	123	223	111	
7	110	219	211	124	224	112	
8	110	219	212	125	225	113	
9	110	219	213	126	226	114	
10	110	219	214	127	227	115	
11	110	219	215	128	228	116	
12	110	219	216	129	229	117	
13	110	219	204	130	230	104	Side Span
14	110	219	203	131	231	103	
15	110	219	202	132	232	102	
16	110	219	201	133	233	101	

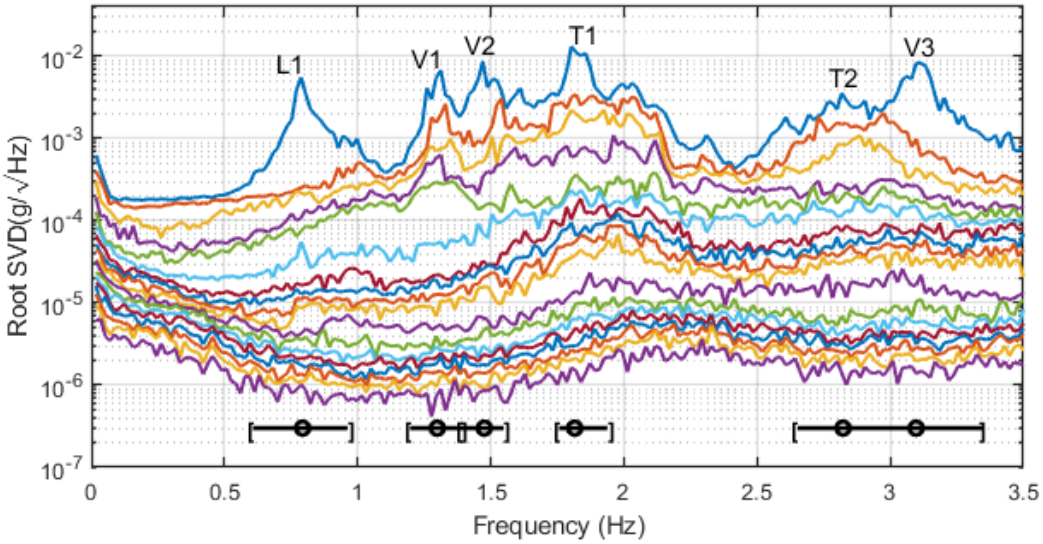

Figure 7 SV spectrum, Setup 1, Queen's park footbridge

Table 8 Identified natural frequencies and damping ratios

Setup	f (Hz)						ζ (%)					
	L1	V1	V2	T1	T2	V3	L1	V1	V2	T1	T2	V3
1	0.808	1.306	1.488	1.821	2.843	3.119	2.3	0.9	1.9	0.7	2.8	1.4
2	0.804	1.305	1.484	1.813	2.835	3.104	1.7	1.3	3.0	1.9	2.6	1.7
3	0.795	1.301	1.478	1.825	2.852	3.100	2.0	0.9	1.7	0.9	2.1	0.9
4	0.771	1.303	1.469	1.799	2.821	3.089	1.6	0.8	1.1	1.4	1.3	1.3
5	0.782	1.296	1.474	1.814	2.817	2.981	2.1	1.5	1.8	1.4	1.1	1.1
6	0.776	1.301	1.481	1.780	2.803	2.967	3.1	0.6	1.7	1.1	0.8	0.9
7	0.761	1.305	1.493	1.810	2.816	3.099	1.3	0.8	2.8	1.8	0.6	0.9
8	0.794	1.304	1.478	1.800	2.792	3.112	2.8	0.8	2.2	0.9	1.0	1.2
9	0.773	1.302	1.466	1.797	2.811	3.095	2.1	0.7	1.6	1.5	1.1	1.6
10	0.774	1.299	1.463	1.786	2.804	3.105	2.8	0.6	1.4	0.8	1.7	1.1
11	0.761	1.307	1.464	1.794	2.799	2.999	2.7	0.9	2.1	0.8	1.0	2.4
12	0.783	1.303	1.469	1.794	2.788	3.009	3.8	0.8	1.1	0.9	1.1	1.6
13	0.781	1.301	1.467	1.784	2.793	3.092	3.4	0.9	1.1	1.6	1.2	1.1
14	0.756	1.299	1.460	1.788	2.801	3.089	4.0	1.0	2.4	1.7	1.5	0.9
15	0.753	1.305	1.463	1.791	2.770	3.066	1.9	1.0	1.5	2.5	1.6	2.0
16	0.767	1.306	1.462	1.783	2.785	3.077	3.0	0.7	1.0	2.5	1.2	1.5
Mean	0.777	1.303	1.472	1.799	2.808	3.069	2.5	0.9	1.8	1.4	1.4	1.4
c.o.v. (%)	2.1	0.2	0.7	0.8	0.8	1.6	31.5	24.7	34.4	41.0	44.5	31.9

Table 8 and Table 9 summarise the MPV of modal parameters in different setups. The MPVs of each parameter in different setups are close but not identical as expected. The bottom two rows of the tables give the sample mean and coefficient of variation (c.o.v. = standard deviation/mean) of the MPVs calculated based on the samples among the setups. The c.o.v. of natural frequencies is typically small (< 3%) while that of other parameters are relatively larger (in the order of a few tens of percent). In particular, the sample c.o.v.s of modal force PSD and PSD of prediction error reflect the variation of the environmental condition during the test.

Table 9 Identified modal force PSD and prediction error PSD

Setup	$\sqrt{S_{ii}}\left(100\times\mu g/\sqrt{Hz}\right)$						$\sqrt{S_e}\left(100\times\mu g/\sqrt{Hz}\right)$					
	L1	V1	V2	T1	T2	V3	L1	V1	V2	T1	T2	V3
1	6.0	3.5	6.1	7.1	4.6	4.1	0.6	3.9	3.0	6.7	1.9	1.9
2	7.4	4.9	10.1	17.8	4.6	4.5	0.6	4.5	3.6	9.8	2.6	2.6
3	6.3	4.0	7.8	7.4	4.0	5.4	0.6	4.0	4.4	9.1	2.9	2.9
4	6.7	4.0	8.5	7.5	2.7	4.5	0.6	4.8	5.8	7.4	1.4	1.4
5	6.6	5.5	7.4	11.9	3.4	11.6	0.6	5.9	5.4	12.1	3.6	3.6
6	5.6	3.1	9.8	9.0	4.2	13.3	0.5	6.4	5.5	10.0	4.4	4.4
7	6.0	4.0	17.6	11.2	2.5	5.6	0.6	6.6	11.0	9.1	1.9	1.9
8	7.4	2.5	5.1	13.6	3.4	4.5	0.9	4.1	5.0	14.5	2.3	2.3
9	6.9	3.5	8.0	11.7	3.5	5.3	0.6	4.9	4.8	11.3	1.9	1.9
10	7.3	3.6	3.7	9.8	2.6	5.3	0.6	5.0	2.9	7.2	1.5	1.5
11	6.3	4.8	11.2	9.5	3.5	11.1	0.4	4.1	5.5	10.1	2.1	2.1
12	6.6	2.3	4.9	10.6	4.0	11.8	0.6	2.7	2.6	9.3	1.9	1.9
13	7.9	3.8	6.3	13.4	3.7	5.3	0.4	2.3	2.6	5.6	0.9	0.9
14	5.4	3.3	6.3	17.8	3.4	4.1	0.4	2.4	2.3	4.8	0.6	0.6
15	6.9	6.7	12.3	21.9	4.6	17.4	0.5	3.2	4.0	5.5	1.4	1.4
16	7.7	4.9	6.3	23.1	3.8	6.0	0.6	3.1	2.9	5.4	0.7	0.7
Mean	6.7	4.0	8.2	12.7	3.7	7.5	0.5	4.2	4.5	8.6	2.0	2.0
c.o.v. (%)	10.9	27.8	41.8	39.3	18.1	55.1	23.9	31.1	47.8	31.6	51.0	51.0

Figure 8 shows the identified mode shapes of these six modes. The red and black lines indicate respectively the undeformed and deformed shape. Mode L1 is a symmetric bending mode along the transverse direction. It can be seen that the support restraints the motion at the tower locations. There is also a slight torsional vibration from the x-z view. Modes V1 and V2 are the symmetric and asymmetric vertical modes, respectively. Mode T1 is a torsional mode with a slight transverse motion while T2 is a combination of torsional and symmetric transverse

modes. Mode V3 is the third vertical mode. For all the modes, the mode shape values at the side spans are practically zero, indicating that the main span vibrates independently of the side ones. This checks with visual inspection of the structure that suggested no connection between the main and side spans. Although there is no exact answer for comparison, the identified mode shapes look reasonable and physically make sense. A thorough comparison with three existing methods is provided in the following section.

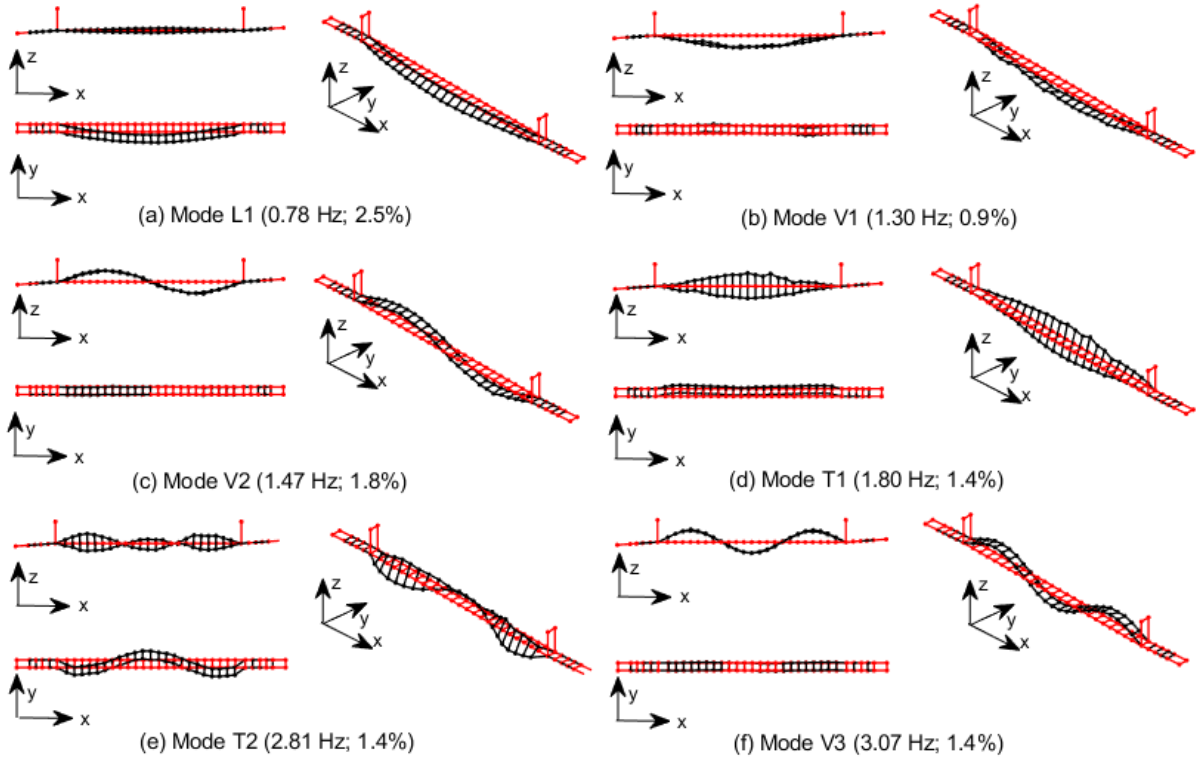

Figure 8 Identified mode shapes; Queen's park footbridge

The computational time for identifying the modal parameters in the two examples is discussed here. The calculation was performed using Matlab R2016a on an HP EliteDesk 800 G2 desktop (Intel Core i5, 3.20 GHz and 8GB of RAM). In general, the time required for convergence increases with the number of setups and the number of modes in the selected band. This is essentially because the number of parameters increases accordingly. The convergence tolerance in the iteration was set to be 10^{-5} on a fractional basis for all the modal parameters.

Table 10 shows the computational time for the shear building and footbridge examples. Except for Modes {V2} and {T2, V3}in the field test example, the MPVs can be determined in less than half a minute. Mode {V2} requires longer time (around one minute) to converge, possibly due to the lower s/n ratio in some setups. The longest time (138.9 s) is required for the close modes {T2, V3}. Nevertheless, it is still acceptable even on site.

Table 10 Computational time

Example	Mode	No. of iterations	Time required (s)
Shear Building	{TX1, TY1, R1}	89	21.5
(synthetic data)	{TX2, TY3}	86	15.6
	{R2}	38	3.7
Footbridge (field data)	{L1}	30	15.0
	{V1}	50	15.4
	{V2}	150	60.8
	{T1}	55	20.1
	{T2, V3}	126	138.9

5.3. Comparison with existing methods

Since the 'true' values of modal parameters in the field test of the suspension footbridge are unknown, the results identified in Section 5.2 are compared with those by three existing methods, namely, the modular SSI [23] and two post-identification approaches based on Frequency Domain Decomposition (FDD) [45] and Bayesian single-setup algorithm [33]. These three algorithms are well established and are sufficient to check the performance of the proposed algorithm, especially when there are challenges encountered in practical situations.

The modular SSI is one of the pre-identification methods for multiple setup measurements. It allows one to process all the setups simultaneously and extracts the modal parameters from a global subspace matrix which contains all measured setups. A MATLAB implementation of this method [46] is used in this study. For the FDD and the Bayesian single-setup algorithm, we apply the post-identification approach, that is, the local mode shapes in each setup are identified by FDD or Bayesian method first and the global mode shapes are then assembled using least squares method. Conventionally, the local least squares method is employed to produce the global mode shapes, e.g., in Section 11.3.1 of [2], but here we adopt the global least squares method [19] as it eliminates the choice of reference setup by minimising a global measure-of-fit function.

Table 11 compares the identified natural frequencies and damping ratios by different methods, where the results obtained by the proposed algorithm and FDD are reported in terms of the sample mean among the setups. The natural frequencies and damping ratios identified by Bayesian single-setup algorithm are practically the same as the proposed algorithm and hence omitted here. It is seen that the results obtained by the proposed algorithm are generally close

to their counterparts by other methods. The frequencies deviate slightly, while the damping ratios are again similar except for the Mode V2 in modular SSI.

Table 11 Comparison of identified natural frequencies and damping ratios between existing and proposed methods

Mode	f (Hz)			ζ (%)		
	proposed	modular SSI	FDD	proposed	modular SSI	FDD
L1	0.777	0.791	0.773	2.5	2.8	2.1
V1	1.303	1.314	1.303	0.9	1.1	1.1
V2	1.472	1.489	1.464	1.8	3.1	1.6
T1	1.799	1.801	1.792	1.4	1.2	1.2
T2	2.808	2.782	2.814	1.4	1.9	0.8
V3	3.069	3.094	3.088	1.4	1.2	1.0

The MACs between the mode shapes identified by the proposed algorithm with respect to the remaining methods are shown in Table 12. All the MACs for Modes L1, V1, T1 and V3 are greater than 0.98, indicating a good consistency of the identified mode shapes. Differences exist in the mode shapes of Modes V2 and T2 produced by the modular SSI, and of the Mode T2 identified by the post-identification methods. For a further comparison, those modes are illustrated in Table 13 taking the x-z view.

Table 12 MAC between the mode shapes identified by the proposed algorithm with respect to the existing methods

Method	L1	V1	V2	T1	T2	V3
Modular SSI	0.9962	0.9840	0.9513	0.9837	0.9608	0.9933
Post-identification approach based on FDD	0.9998	0.9902	0.9960	0.9924	0.9549	0.9980
Post-identification approach based on Bayesian method	1.0000	1.0000	1.0000	1.0000	0.9889	0.9996

Although the MACs between the mode shapes identified are all greater than 95%, they only indicate the overall discrepancy and need not inform the local features. The mode shapes of V2 and T2 produced by modular SSI are ‘noisier’ with kinks at some measured DOFs, which might be due to the low modal s/n ratio at some setups. The mode shapes of V2 identified by the post-identification approaches based on FDD and Bayesian single-setup method are similar to that yielded by the proposed method, but the mode shapes of T2 have more unreasonable kinks, though the one identified by the Bayesian single-setup method looks a little better (kinks appear

in Setup 5). This poor quality of T2 could be due to either the method when identifying the local mode shapes or least squares method when producing the global mode shapes. In the absence of the result produced by the proposed algorithm, it is difficult to determine whether such kinks are due to structural behaviour or merely computational artifacts. From Table 13, the mode shape of T2 identified by the proposed algorithm is physically more plausible.

Table 13 Comparison of V2 and T2 between existing methods and proposed algorithm

Method	V2	T2
Proposed algorithm (copied from Figure 8)	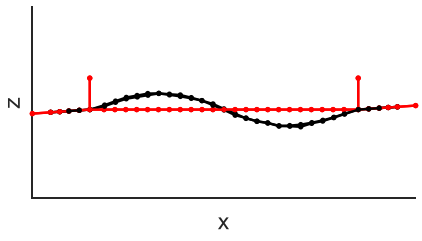	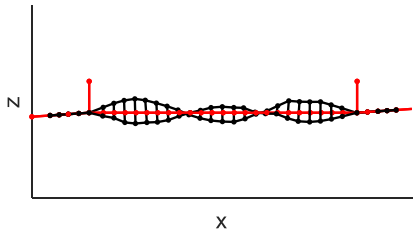
Modular SSI	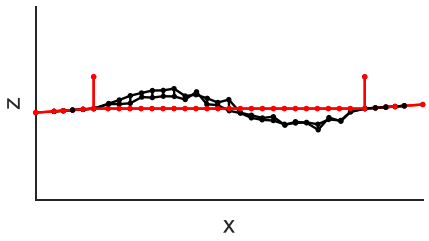	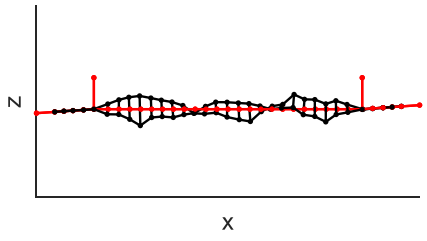
Post-identification approach based on FDD	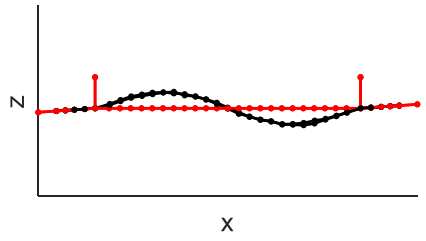	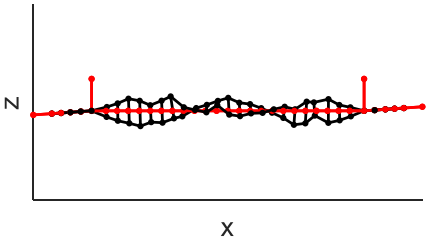
Post-identification approach based on Bayesian method	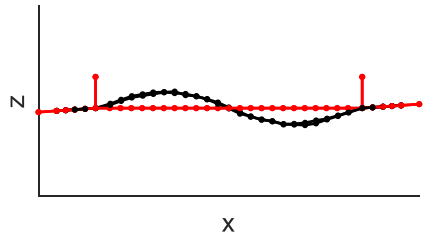	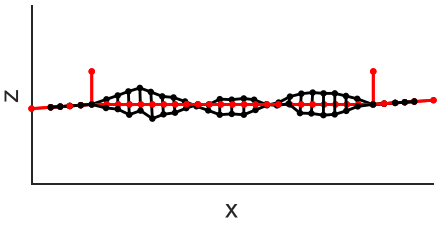

The issue of Mode T2 is further studied to investigate the factors that influence the quality of the assembled mode shape. The previous study [25] revealed that significant disagreement in the identified mode shape values at the reference DOFs among different setups can present challenge for least squares method, be it local or global. Figure 9 shows the MAC between the mode shape values of T2 at the reference locations identified using the data in Setup 5 and

other setups by Bayesian single-setup algorithm. The closer the MAC is to 1, the better the agreement. It is seen that all the MAC values are above 0.90, indicating that the mode shape identified in Setup 5 agrees well with that in other setups at the reference locations. This is also true between any other setups, hence the reason for the poor quality of mode shape of T2 may differ from that in [25]. Figure 10 shows the time history of the data collected in one of the vertical data channels in Setup 5. It is seen from Figure 10(b) that the measured response follows a sinusoidal wave with a frequency around 3 Hz from 870 s to 900 s, which is possibly due to jogging activities on the bridge during this period. The interference is within the selected frequency band of mode T2 and V3. If we exclude the portion of data between 870 s and 900 s for modal identification, then the mode shape assembled by global least squares method with Bayesian method (see Figure 11(a)) will be of better quality compared to the original mode shape and consistent with that by the proposed algorithm. This implies that the interference from this portion of data is significant for global least squares method but not so for the proposed method, hence the proposed method is more robust to the data quality. The global least squares method tries to fit the theoretical mode shapes with equal weights based on the most probable mode shapes identified individually in each setup, which involves different levels of noise and violation of assumptions. Estimation error of the mode shape in the problematic setup will smear into the assembled counterpart and even affect other originally well-identified setups. Identifying the global mode shapes in a Bayesian manner seems to automatically place the ‘weights’ in different setups based on their data quality, allowing the information in different setups to ‘correct’ the mode shape values in the problematic setups.

For both the modular SSI and the post-identification approach based on FDD as seen in Figure 11(b) and (c), the mode shapes of T2 are still problematic even when the portion of data between 870 s and 900 s is excluded for modal identification. This is possibly due to the low s/n ratio of Mode T2 (see Figure 7), which reduces the quality of identified mode shapes.

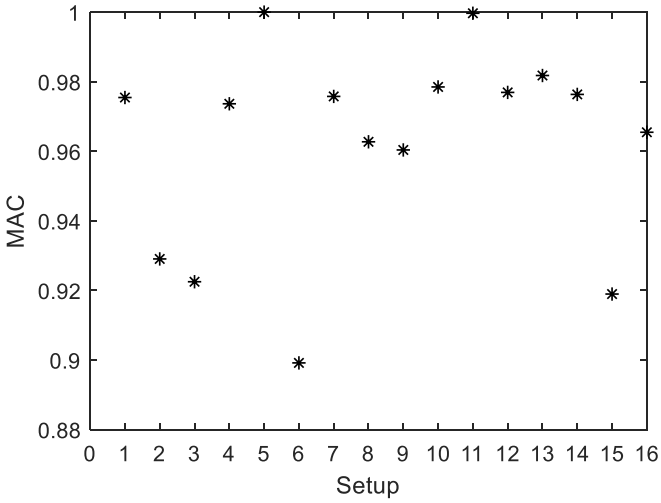

Figure 9 MAC between the mode shape values of T2 at the reference locations identified using the data in Setup 5 and other setups

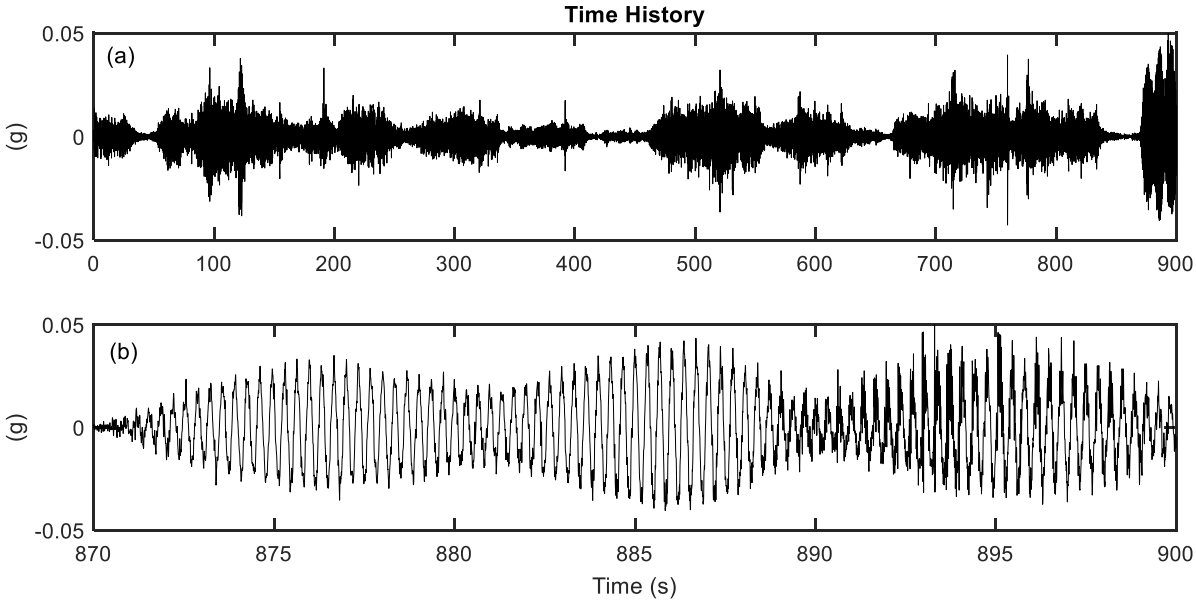

Figure 10 Time history of one of the vertical channels in Setup 5 (a) from 0 to 900 s; (b) zoom into the segment from 870 s to 900 s

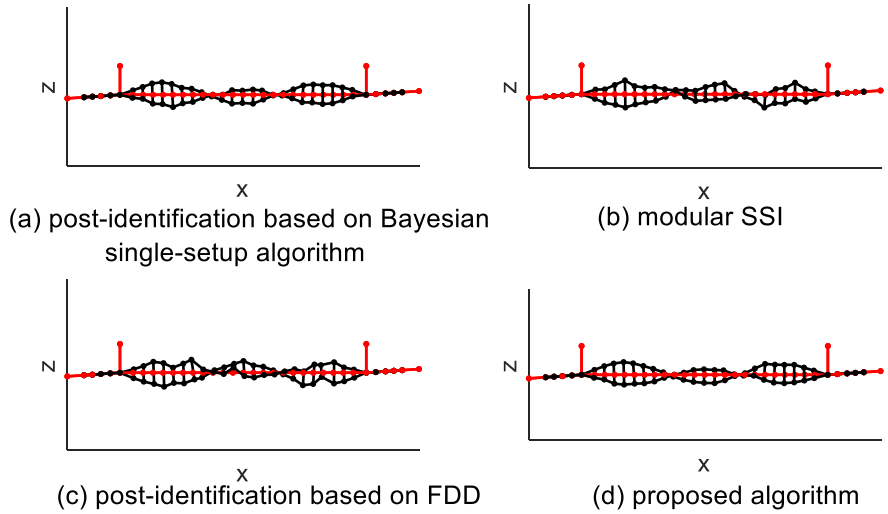

Figure 11 Identified mode shape of T2 by existing methods (a) – (c) when excluding the portion of data between 870 s and 900 s in Setup 5; and by the proposed algorithm (d) copied from Figure 8(e)

6. Conclusions

This paper has developed a fast Bayesian FFT method based on the P-EM algorithm for modal identification incorporating multiple setups. It provides a fundamental means to process the information from multiple setup measurements strictly consistent with modelling assumptions and probability logic without heuristics. The modal parameters (except the mode shape) in different setups are not constrained to be the same. This allows for more robustness in the identification model. The computational difficulties are addressed by the P-EM algorithm. Except for the natural frequencies and damping ratios, analytical formulae have been derived for updating the modal parameters, leading to a fast iterative procedure that is also elegant and conducive to computer coding. The proposed method is applicable for the general case of multiple (possibly close) modes even with a large number of measured DOFs. Two examples have been presented to demonstrate the consistency and feasibility of the method.

Focusing on the global mode shape, a critical comparison was made between the proposed algorithm and three common existing methods. It is found that for modes with high modal s/n ratios in all setups, the assembled mode shape is insensitive to the choice of method. Challenges exist when the data quality is poor in some setups. The proposed Bayesian method is found to be more robust to modal s/n ratio, producing a global mode shape that is physically sound.

7. Supplementary data

Supplementary data to this article can be accessed by contacting zhuzuo@liverpool.ac.uk.

8. Acknowledgements

This work is funded by the UK Engineering & Physical Sciences Research Council (EP/N017897/1). In addition, the first author is supported by the Joint University of Liverpool/China Scholarship Council Scholarship, the second author by grant SUG/4 at the Nanyang Technological University, Singapore, the third and fourth authors by the ZJU-UIUC Institute of Zhejiang University (130000-171207704/018). The authors also would like to thank Ms. Xinrui Wang at the University of Liverpool for participating in the field test of the Queen's Park bridge.

9. Appendix A. Derivations for Section 4

In this appendix, we provide the derivations for some expressions in Section 4, i.e., the complete log-likelihood function in (14), the closed-form update of modal force PSD in (27), the alternative form of LLF in (30) and the initial guess of modal force PSD in (35).

Complete log-likelihood function in (14)

The derivation here is similar to Appendix B.1 of [34] although it is presented for the present case of multiple setup data for completeness. Based on the theory of multivariate complex Guassian distribution and (13), the $\hat{\mathcal{F}}_k^{(r)}$ given $\boldsymbol{\eta}_k^{(r)}$ follows the complex Guassian distribution with the mean and covariance as follows:

$$E\left(\hat{\mathcal{F}}_k^{(r)}\middle|\boldsymbol{\eta}_k^{(r)},\boldsymbol{\theta}^{(r)}\right)=\boldsymbol{\Phi}_r\boldsymbol{\eta}_k^{(r)} \tag{36}$$

$$\mathbf{C}\left[\hat{\mathcal{F}}_k^{(r)}\middle|\boldsymbol{\eta}_k^{(r)},\boldsymbol{\theta}^{(r)}\right]=S_e^{(r)}\mathbf{I}_{n_r} \tag{37}$$

Since $\boldsymbol{\eta}_k^{(r)}\middle|\boldsymbol{\theta}^{(r)}\sim CN\left(\mathbf{0},\mathbf{H}_k^{(r)}\right)$, one can obtain the complete-data log likelihood function

$$
\begin{aligned}
&L\left(\boldsymbol{\theta};\left\{\hat{\mathcal{F}}_k^{(r)},\boldsymbol{\eta}_k^{(r)}\right\}\right)=\sum_{r=1}^{n_s}\sum_k \log p\left(\hat{\mathcal{F}}_k^{(r)},\boldsymbol{\eta}_k^{(r)}\middle|\boldsymbol{\theta}\right)\\
&=\sum_{r=1}^{n_s}\sum_k \log\left[\, p\left(\hat{\mathcal{F}}_k^{(r)}\middle|\boldsymbol{\eta}_k^{(r)},\boldsymbol{\theta}\right)p\left(\boldsymbol{\eta}_k^{(r)}\middle|\boldsymbol{\theta}\right)\right]=\sum_{r=1}^{n_s}\sum_k \log p\left(\hat{\mathcal{F}}_k^{(r)}\middle|\boldsymbol{\eta}_k^{(r)},\boldsymbol{\theta}\right)+\sum_{r=1}^{n_s}\sum_k \log p\left(\boldsymbol{\eta}_k^{(r)}\middle|\boldsymbol{\theta}\right) \qquad (38)\\
&=\sum_{r=1}^{n_s} L_r
\end{aligned}
$$

where

$$
\begin{aligned}
&L_r=-\left(n_r+m\right)N_f^{(r)}\ln\pi-n_r N_f^{(r)}\ln S_e^{(r)}-S_e^{(r)-1}\sum_k\left[\hat{\mathcal{F}}_k^{(r)}-\boldsymbol{\Phi}_r\boldsymbol{\eta}_k^{(r)}\right]^*\left[\hat{\mathcal{F}}_k^{(r)}-\boldsymbol{\Phi}_r\boldsymbol{\eta}_k^{(r)}\right]\\
&+\sum_k\ln\left|\mathbf{H}_k^{(r)-1}\right|-\sum_k\boldsymbol{\eta}_k^{(r)*}\mathbf{H}_k^{(r)-1}\boldsymbol{\eta}_k^{(r)}
\end{aligned}
\qquad (39)
$$

Closed-form update of modal force PSD in (27)

Substituting the expression of $\mathbf{H}_k^{(r)}=\mathbf{h}_k^{(r)}\mathbf{S}^{(r)}\mathbf{h}_k^{(r)*}$ into (20) and rearranging gives

$$
Q_2^{(r)}\left(\boldsymbol{\theta}\middle|\boldsymbol{\theta}^{(t)}\right)=\sum_k\ln\left|\mathbf{h}_k^{(r)-*}\mathbf{h}_k^{(r)-1}\right|+\sum_k\ln\left|\mathbf{S}^{(r)-1}\right|-tr\left(\sum_k\mathbf{S}^{(r)-1}\mathbf{h}_k^{(r)-1}\mathbf{w}_{2k}^{(r)}\mathbf{h}_k^{(r)-*}\right) \qquad (40)
$$

Note that $\mathbf{S}^{(r)}$ is only involved in $Q_2^{(r)}\left(\boldsymbol{\theta}\middle|\boldsymbol{\theta}^{(t)}\right)$ in (18). Taking the partial derivative of $Q\left(\boldsymbol{\theta}\middle|\boldsymbol{\theta}^{(t)}\right)$ in (18) with respect to $\mathrm{Re}\,\mathbf{S}^{(r)-1}$ gives

$$
\begin{aligned}
&\partial Q\left(\boldsymbol{\theta}\middle|\boldsymbol{\theta}^{(t)}\right)/\partial\,\mathrm{Re}\,\mathbf{S}^{(r)-1}=\partial Q_2^{(r)}\left(\boldsymbol{\theta}\middle|\boldsymbol{\theta}^{(t)}\right)/\partial\,\mathrm{Re}\,\mathbf{S}^{(r)-1}\\
&=N_f^{(r)}\left(2\,\mathrm{Re}\,\mathbf{S}^{(r)}-\mathrm{Re}\,\mathbf{S}^{(r)}\odot\mathbf{I}_{n_r}\right)-\sum_k\left(2\,\mathrm{Re}\left(\mathbf{h}_k^{(r)-1}\mathbf{w}_{2k}^{(r)}\mathbf{h}_k^{(r)-*}\right)-\mathrm{Re}\left(\mathbf{h}_k^{(r)-1}\mathbf{w}_{2k}^{(r)}\mathbf{h}_k^{(r)-*}\right)\odot\mathbf{I}_{n_r}\right)
\end{aligned}
\qquad (41)
$$

where '$\odot$' denotes matrix elements product (also known as Hadamard product).

Setting (41) to be zero yields

$$
\mathrm{Re}\left(\mathbf{S}^{(r)}\right)=\frac{1}{N_f^{(r)}}\mathrm{Re}\left[\sum_k\left(\mathbf{h}_k^{(r)-1}\mathbf{w}_{2k}^{(r)}\mathbf{h}_k^{(r)-*}\right)\right] \qquad (42)
$$

Similarly, one can have

$$
\mathrm{Im}\left(\mathbf{S}^{(r)}\right)=\frac{1}{N_f^{(r)}}\mathrm{Im}\left[\sum_k\left(\mathbf{h}_k^{(r)-1}\mathbf{w}_{2k}^{(r)}\mathbf{h}_k^{(r)-*}\right)\right] \qquad (43)
$$

Combining (42) and (43) gives

$$\mathbf{S}^{(r)} = \frac{1}{N_f^{(r)}} \sum_k \left(\mathbf{h}_k^{(r)-1} \mathbf{w}_{2k}^{(r)} \mathbf{h}_k^{(r)-*} \right) \tag{44}$$

Alternative form of LLF in (30)

For the purpose of deriving (30), we first introduce the Matrix Inverse Lemma and Matrix Determinant Theorem [40].

1. Matrix Inverse Lemma

For any complex matrices *A, C, U, V* of appropriate size, with *A* and *C* invertible,

$$\left(A + UCV\right)^{-1} = A^{-1} - A^{-1}U\left(C^{-1} + VA^{-1}U\right)^{-1}VA^{-1} \tag{45}$$

2. Matrix determinant theorem

For any complex matrices *A, C, U, V* of appropriate size, with *A* and *C* invertible,

$$\det\left(A + UCV\right) = \left(\det A\right)\left(\det C\right)\det\left(C^{-1} + VA^{-1}U\right) \tag{46}$$

Based on (45), the inverse of $\mathbf{E}_k^{(r)}$ can be re-written as

$$\begin{aligned} \mathbf{E}_k^{(r)-1} &= \left(\mathbf{\Phi}_r \mathbf{H}_k^{(r)} \mathbf{\Phi}_r^T + S_e^{(r)} \mathbf{I}_{n_r}\right)^{-1} \\ &= S_e^{(r)-1} \mathbf{I}_{n_r} - S_e^{(r)-1} \mathbf{\Phi}_r \left[S_e^{(r)-1} \mathbf{\Phi}_r^T \mathbf{\Phi}_r + \mathbf{H}_k^{(r)-1} \right]^{-1} \mathbf{\Phi}_r^T S_e^{(r)-1} \\ &= S_e^{(r)-1} \mathbf{I}_{n_r} - S_e^{(r)-1} \mathbf{\Phi}_r \mathbf{J}_k^{(r)-1} \mathbf{\Phi}_r^T \end{aligned} \tag{47}$$

Based on (46), one can re-written the determinant of $\mathbf{E}_k^{(r)}$ as

$$\left|\mathbf{E}_k^{(r)}\right| = S_e^{n_r - m} \left|\mathbf{H}_k^{(r)}\right| \left|\mathbf{J}_k^{(r)}\right| \tag{48}$$

Substituting (47) and (48) into (10), after rearranging, one can get (30).

Initial guess for modal force PSD in (35)

Taking the partial derivative of L_r in (33) with respect to $\mathrm{Re}\,\mathbf{S}^{(r)-1}$

$$\begin{aligned} &\frac{\partial L_r\left(\boldsymbol{\theta}\right)}{\partial \mathrm{Re}\,\mathbf{S}^{(r)-1}} \sim \sum_k \left(2\,\mathrm{Re}\,\mathbf{S}^{(r)} - \mathrm{Re}\,\mathbf{S}^{(r)} \odot \mathbf{I}\right) - \\ &\sum_k \begin{pmatrix} 2\,\mathrm{Re}\left(\left(\mathbf{h}_k^{(r)}\right)^{-1} \left(\mathbf{\Phi}_r^T \mathbf{\Phi}_r\right)^{-1} \mathbf{\Phi}_r^T \mathcal{F}_k^{(r)} \mathcal{F}_k^{(r)*} \mathbf{\Phi}_r \left(\mathbf{\Phi}_r^T \mathbf{\Phi}_r\right)^{-1} \left(\mathbf{h}_k^{(r)*}\right)^{-1}\right) \\ -\mathrm{Re}\left(\left(\mathbf{h}_k^{(r)}\right)^{-1} \left(\mathbf{\Phi}_r^T \mathbf{\Phi}_r\right)^{-1} \mathbf{\Phi}_r^T \mathcal{F}_k^{(r)} \mathcal{F}_k^{(r)*} \mathbf{\Phi}_r \left(\mathbf{\Phi}_r^T \mathbf{\Phi}_r\right)^{-1} \left(\mathbf{h}_k^{(r)*}\right)^{-1}\right) \odot \mathbf{I} \end{pmatrix} \end{aligned} \tag{49}$$

Then taking the partial derivative of L_r with respect to $\mathrm{Im}\mathbf{S}^{(r)-1}$

$$\frac{\partial L_r(\boldsymbol{\theta})}{\partial \mathrm{Im}\mathbf{S}^{(r)-1}} \sim \sum_k \left(2\,\mathrm{Im}\mathbf{S}^{(r)}\right) - \sum_k \left(2\,\mathrm{Im}\left(\left(\mathbf{h}_k^{(r)}\right)^{-1}\left(\boldsymbol{\Phi}_r^T\boldsymbol{\Phi}_r\right)^{-1}\boldsymbol{\Phi}_r^T\mathcal{F}_k^{(r)}\mathcal{F}_k^{(r)*}\boldsymbol{\Phi}_r\left(\boldsymbol{\Phi}_r^T\boldsymbol{\Phi}_r\right)^{-1}\left(\mathbf{h}_k^{(r)*}\right)^{-1}\right)\right) \tag{50}$$

Setting (49) and (50) to be zero, after rearranging, one can obtain (35).

10. Appendix B. Derivatives of Q-function

This Appendix presents the derivatives of Q-function in (18) with respect to $\left\{f_i^{(r)}\right\}$ and $\left\{\zeta_i^{(r)}\right\}$ required in Newton's method. For convenience, we express the Q-function in (18) as

$$Q\left(\boldsymbol{\theta}\middle|\boldsymbol{\theta}^{(t)}\right) = \sum_{r=1}^{n_s}\left\{Q_{SP}^{(r)}\left(\boldsymbol{\theta}\middle|\boldsymbol{\theta}^{(t)}\right) + Q_{21}^{(r)}\left(\boldsymbol{\theta}\middle|\boldsymbol{\theta}^{(t)}\right) + Q_{23}^{(r)}\left(\boldsymbol{\theta}\middle|\boldsymbol{\theta}^{(t)}\right)\right\} \tag{51}$$

where

$$Q_{SP}^{(r)}\left(\boldsymbol{\theta}\middle|\boldsymbol{\theta}^{(t)}\right) = \sum_{r=1}^{n_s}\left\{-\left(n_r+m\right)N_f^{(r)}\ln\pi - n_r N_f^{(r)}\ln S_e^{(r)} - S_e^{(r)-1}Q_1^{(r)}\left(\boldsymbol{\theta}\middle|\boldsymbol{\theta}^{(t)}\right) + \sum_k \ln\left|\mathbf{S}^{(r)-1}\right|\right\} \tag{52}$$

$$Q_{21}^{(r)}\left(\boldsymbol{\theta}\middle|\boldsymbol{\theta}^{(t)}\right) = \sum_k\sum_{i=1}^{m}\ln D_{ik}^{(r)} \tag{53}$$

$$Q_{23}^{(r)}\left(\boldsymbol{\theta}\middle|\boldsymbol{\theta}^{(t)}\right) = -tr\left(\sum_k \tilde{\mathbf{S}}^{(r)-1}\mathbf{h}_k^{(r)-1}\mathbf{w}_{2k}^{(r)}\mathbf{h}_k^{(r)-*}\right) \tag{54}$$

$$D_{ik}^{(r)} = \left(1+\left(4\zeta_i^{(r)2}-2\right)\beta_{ik}^{(r)2}+\beta_{ik}^{(r)4}\right)^{-1} \tag{55}$$

Note that only the last two terms in (51) involve $\left\{f_i^{(r)}\right\}$ and $\left\{\zeta_i^{(r)}\right\}$. Taking the partial derivative of Q-function with respect to $f_i^{(r)}$ gives

$$\begin{aligned}\frac{\partial Q\left(\boldsymbol{\theta}\middle|\boldsymbol{\theta}^{(t)}\right)}{\partial f_i} &= \frac{\partial Q_{21}^{(r)}\left(\boldsymbol{\theta}\middle|\boldsymbol{\theta}^{(t)}\right)}{\partial f_i} + \frac{\partial Q_{23}^{(r)}\left(\boldsymbol{\theta}\middle|\boldsymbol{\theta}^{(t)}\right)}{\partial f_i} = \sum_k\left(\frac{\partial D_{ik}^{(r)-1}}{\partial f_i}D_{ik}^{(r)}\right) - 2\sum_k tr\left(\mathrm{Re}\left(\mathbf{S}^{(r)-1}\mathbf{h}_k^{(r)-1}\mathbf{w}_{2k}^{(r)}\frac{\partial \mathbf{h}_k^{(r)-*}}{\partial f_i}\right)\right) \\ &= \sum_k\left(\frac{\partial D_{ik}^{(r)-1}}{\partial f_i}D_{ik}\right) - 2\sum_k \mathrm{Re}\left(e_i^T\mathbf{S}^{(r)-1}\mathbf{h}_k^{(r)-1}\mathbf{w}_{2k}^{(r)}e_i\frac{\partial \bar{h}_{ik}^{(r)-1}}{\partial f_i}\right)\end{aligned} \tag{56}$$

where e_i is an m-by-1 vector with the i-th entry equal to 1 and all others equal to 0. $\bar{h}_{ik}^{(r)}$ is the complex transpose of $h_{ik}^{(r)}$. The derivatives of $D_{ik}^{(r)-1}$ and $\bar{h}_{ik}^{(r)-1}$ will be given later.

Similarly, one can have

$$\frac{\partial Q\left(\boldsymbol{\theta}\middle|\boldsymbol{\theta}^{(t)}\right)}{\partial \zeta_i^{(r)}} = \sum_k \left(\frac{\partial D_{ik}^{(r)-1}}{\partial \zeta_i^{(r)}} D_{ik}^{(r)} \right) - 2\sum_k \mathrm{Re}\left(e_i^T \mathbf{S}^{(r)-1} \mathbf{h}_k^{(r)-1} \mathbf{w}_{2k}^{(r)} e_i \frac{\partial \bar{h}_{ik}^{(r)-1}}{\partial \zeta_i^{(r)}} \right) \tag{57}$$

Taking the second partial derivative of Q-function with respect to $f_i^{(r)}$ gives

$$\begin{aligned}
&\frac{\partial Q\left(\boldsymbol{\theta}\middle|\boldsymbol{\theta}^{(t)}\right)}{\partial f_i^{(r)2}} = \frac{\partial Q_{21}^{(r)}\left(\boldsymbol{\theta}\middle|\boldsymbol{\theta}^{(t)}\right)}{\partial f_i^{(r)2}} + \frac{\partial Q_{23}^{(r)}\left(\boldsymbol{\theta}\middle|\boldsymbol{\theta}^{(t)}\right)}{\partial f_i^{(r)2}} \\
&= \sum_k \left(\frac{\partial^2 D_{ik}^{(r)-1}}{\partial f_i^{\,2}} D_{ik}^{(r)} + \left(\frac{\partial D_{ik}^{(r)-1}}{\partial f_i} \right) \left(\frac{\partial D_{ik}^{(r)}}{\partial f_i} \right) \right) - 2\sum_k tr\left(\mathrm{Re}\left(\mathbf{S}^{(r)-1} \frac{\partial \mathbf{h}_k^{(r)-1}}{\partial f_i} \mathbf{w}_{2k}^{(r)} \frac{\partial \mathbf{h}_k^{(r)-*}}{\partial f_i} + \mathbf{S}^{(r)-1} \mathbf{h}_k^{(r)-1} \mathbf{w}_{2k}^{(r)} \frac{\partial \mathbf{h}_k^{(r)-*}}{\partial f_i^{\,2}} \right) \right) \\
&= \sum_k \left(\frac{\partial^2 D_{ik}^{(r)-1}}{\partial f_i^{\,2}} D_{ik}^{(r)} + \left(\frac{\partial D_{ik}^{(r)-1}}{\partial f_i} \right) \left(\frac{\partial D_{ik}^{(r)}}{\partial f_i} \right) \right) - 2\sum_k \mathrm{Re}\left(e_i^T \mathbf{S}^{(r)-1} e_i e_i^T \mathbf{w}_{2k}^{(r)} e_i \frac{\partial h_{ik}^{(r)-1}}{\partial f_i} \frac{\partial \bar{h}_{ik}^{(r)-1}}{\partial f_i} + e_i^T \mathbf{S}^{(r)-1} \mathbf{h}_k^{(r)-1} \mathbf{w}_{2k}^{(r)} e_i \frac{\partial \bar{h}_{ik}^{(r)-1}}{\partial f_i^{\,2}} \right)
\end{aligned} \tag{58}$$

Similarly,

$$\begin{aligned}
&\frac{\partial Q\left(\boldsymbol{\theta}\middle|\boldsymbol{\theta}^{(t)}\right)}{\partial \zeta_i^{(r)2}} = \sum_k \left(\frac{\partial^2 D_{ik}^{(r)-1}}{\partial \zeta_i^{(r)2}} D_{ik}^{(r)} + \left(\frac{\partial D_{ik}^{(r)-1}}{\partial \zeta_i^{(r)}} \right) \left(\frac{\partial D_{ik}^{(r)}}{\partial \zeta_i^{(r)}} \right) \right) \\
&-2\sum_k \mathrm{Re}\left(e_i^T \mathbf{S}^{(r)-1} e_i e_i^T \mathbf{w}_{2k}^{(r)} e_i \frac{\partial h_{ik}^{(r)-1}}{\partial \zeta_i^{(r)}} \frac{\partial \bar{h}_{ik}^{(r)-1}}{\partial \zeta_i^{(r)}} + e_i^T \mathbf{S}^{(r)-1} \mathbf{h}_k^{(r)-1} \mathbf{w}_{2k}^{(r)} e_i \frac{\partial \bar{h}_{ik}^{(r)-1}}{\partial \zeta_i^{(r)2}} \right)
\end{aligned} \tag{59}$$

$$\begin{aligned}
&\frac{\partial Q\left(\boldsymbol{\theta}\middle|\boldsymbol{\theta}^{(t)}\right)}{\partial f_i^{(r)} \partial \zeta_i^{(r)}} = \sum_k \left(\frac{\partial^2 D_{ik}^{(r)-1}}{\partial f_i^{(r)} \partial \zeta_i^{(r)}} D_{ik}^{(r)} + \left(\frac{\partial D_{ik}^{(r)-1}}{\partial f_i^{(r)}} \right) \left(\frac{\partial D_{ik}^{(r)}}{\partial \zeta_i^{(r)}} \right) \right) \\
&-2\sum_k \mathrm{Re}\left(e_i^T \mathbf{S}^{(r)-1} e_i e_i^T \mathbf{w}_{2k}^{(r)} e_i \frac{\partial h_{ik}^{(r)-1}}{\partial f_i^{(r)}} \frac{\partial \bar{h}_{ik}^{(r)-1}}{\partial \zeta_i^{(r)}} + e_i^T \mathbf{S}^{(r)-1} \mathbf{h}_k^{(r)-1} \mathbf{w}_{2k}^{(r)} e_i \frac{\partial \bar{h}_{ik}^{(r)-1}}{\partial f_i^{(r)} \partial \zeta_i^{(r)}} \right)
\end{aligned} \tag{60}$$

For $i \neq j$,

$$\frac{\partial Q\left(\boldsymbol{\theta}\middle|\boldsymbol{\theta}^{(t)}\right)}{\partial f_i^{(r)} \partial f_j^{(r)}} = -2\sum_k \mathrm{Re}\left(e_i^T \mathbf{S}^{(r)-1} e_j \frac{\partial h_{jk}^{(r)-1}}{\partial f_j^{(r)}} e_j^T \mathbf{w}_{2k}^{(r)} e_i \frac{\partial \bar{h}_{ik}^{(r)-1}}{\partial f_i^{(r)}} \right) \tag{61}$$

$$\frac{\partial Q\left(\boldsymbol{\theta}\middle|\boldsymbol{\theta}^{(t)}\right)}{\partial \zeta_i^{(r)} \partial \zeta_j^{(r)}} = -2\sum_k \mathrm{Re}\left(e_i^T \mathbf{S}^{(r)-1} e_j \frac{\partial h_{jk}^{(r)-1}}{\partial \zeta_j^{(r)}} e_j^T \mathbf{w}_{2k}^{(r)} e_i \frac{\partial \bar{h}_{ik}^{(r)-1}}{\partial \zeta_i^{(r)}} \right) \tag{62}$$

$$\frac{\partial Q\left(\boldsymbol{\theta}\middle|\boldsymbol{\theta}^{(t)}\right)}{\partial f_i^{(r)}\partial \zeta_j^{(r)}} = -2\sum_k \mathrm{Re}\left(e_j^T \mathbf{S}^{(r)-1} e_i e_i^T \mathbf{w}_{2k}^{(r)} e_j \frac{\partial h_{ik}^{(r)-1}}{\partial f_i^{(r)}} \frac{\partial \bar{h}_{jk}^{(r)-1}}{\partial \zeta_j^{(r)}} \right) \tag{63}$$

Equations (56) to (63) involve derivatives of the quantities $D_{ik}^{(r)-1}$ and $h_{ik}^{(r)-*}$ which are presented in the following [41]

$$\frac{\partial D_{ik}^{(r)-1}}{\partial f_i^{(r)}} = 4\beta_{ik}^{(r)} f_k^{(r)-1}\left(\beta_{ik}^{(r)2} - 1 + 2\zeta_i^{(r)2}\right) \quad \frac{\partial D_{ik}^{(r)-1}}{\partial \zeta_i^{(r)}} = 8\beta_{ik}^{(r)2}\zeta_i^{(r)} \tag{64}$$

$$\frac{\partial^2 D_{ik}^{(r)-1}}{\partial f_i^{(r)2}} = 12 f_k^{(r)-2}\beta_{ik}^{(r)2} + 4 f_k^{(r)-2}\left(-1 + 2\zeta_i^{(r)2}\right) \quad \frac{\partial^2 D_{ik}^{(r)-1}}{\partial \zeta_i^{(r)2}} = 8\beta_{ik}^{(r)2} \quad \frac{\partial^2 D_{ik}^{(r)-1}}{\partial f_i^{(r)}\partial \zeta_i^{(r)}} = 16\beta_{ik}^{(r)} f_k^{(r)-1}\zeta_i^{(r)} \tag{65}$$

$$\frac{\partial D_{ik}^{(r)}}{\partial f_i^{(r)}} = -4D_{ik}^{(r)2}\left(\left(2\zeta_i^{(r)2} - 1\right)\beta_{ik}^{(r)} + \beta_{ik}^{(r)3}\right) \quad \frac{\partial D_{ik}^{(r)}}{\partial \zeta_i^{(r)}} = -8\beta_{ik}^{(r)2} D_{ik}^{(r)2}\zeta_i^{(r)} \tag{66}$$

$$\frac{\partial \bar{h}_{ik}^{(r)-1}}{\partial f_i^{(r)}} = -2 f_k^{-1}\left(\beta_{ik}^{(r)} - \zeta_i^{(r)}\mathbf{i}\right) \quad \frac{\partial \bar{h}_{ik}^{(r)-1}}{\partial \zeta_i^{(r)}} = 2\beta_{ik}^{(r)}\mathbf{i} \tag{67}$$

$$\frac{\partial \bar{h}_{ik}^{(r)-1}}{\partial f_i^{(r)2}} = -2 f_k^{-2} \quad \frac{\partial \bar{h}_{ik}^{(r)-1}}{\partial \zeta_i^{(r)2}} = 0 \quad \frac{\partial \bar{h}_{ik}^{(r)-1}}{\partial f_i^{(r)}\partial \zeta_i^{(r)}} = 2 f_k^{-1}\mathbf{i} \tag{68}$$

11. References

[1] Au SK. Operational modal analysis: Modeling, bayesian inference, uncertainty laws. Springer; 2017.

[2] Brincker R, Ventura CE. Introduction to Operational Modal Analysis. John Wiley & Sons; 2015.

[3] Rainieri C, Fabbrocino G. Operational Modal Analysis of Civil Engineering Structures. New York: Springer; 2014.

[4] Au SK, Zhang FL. Ambient modal identification of a primarysecondary structure by Fast Bayesian FFT method. Mech Syst Signal Process 2012;28:280–96.

[5] Brownjohn JMW, Magalhaes F, Caetano E, Cunha A. Ambient vibration re-testing and operational modal analysis of the Humber Bridge. Eng Struct 2010;32:2003–18.

[6] Brownjohn JMW, Au SK, Zhu Y, Sun Z, Li B, Bassitt J, et al. Bayesian operational modal analysis of Jiangyin Yangtze River Bridge. Mech Syst Signal Process

2018;110:210–30.

[7] Lacanna G, Ripepe M, Marchetti E, Coli M, Garzonio CA. Dynamic response of the Baptistery of San Giovanni in Florence, Italy, based on ambient vibration test. J Cult Herit 2016;20:632–40.

[8] Abdulamit A, Demetriu S, Aldea A, Neagu C, Gaftoi D. Ambient Vibration Tests at Some Buttress Dams in Romania. Procedia Eng., 2017.

[9] Chen GW, Omenzetter P, Beskhyroun S. Operational modal analysis of an eleven-span concrete bridge subjected to weak ambient excitations. Eng Struct 2017;151:839–60.

[10] Khiem NT, Toan LK. A novel method for crack detection in beam-like structures by measurements of natural frequencies. J Sound Vib 2014;333:4084–103.

[11] Yin T, Jiang QH, Yuen KV. Vibration-based damage detection for structural connections using incomplete modal data by Bayesian approach and model reduction technique. Eng Struct 2017;132:260–77.

[12] Pandey A, Biswas M, Samman M. Damage Detection From Mode Changes in Curvature. J Sound Vib 1991;145:321–32.

[13] Friswell M, Mottershead JE. Finite Element Model Updating in Structural Dynamics. Springer Science & Business Media; 2013.

[14] Zhang FL, Ni YC, Lam HF. Bayesian structural model updating using ambient vibration data collected by multiple setups. Struct Control Heal Monit 2017;24.

[15] Lam HF, Yang J, Au SK. Bayesian model updating of a coupled-slab system using field test data utilizing an enhanced Markov chain Monte Carlo simulation algorithm. Eng Struct 2015;102:144–55.

[16] Brownjohn JMW. Structural health monitoring of civil infrastructure. Philos Trans R Soc A Math Phys Eng Sci 2007;365:589–622.

[17] Cross EJ, Koo KY, Brownjohn JMW, Worden K. Long-term monitoring and data analysis of the Tamar Bridge. Mech Syst Signal Process 2013;35:16–34.

[18] Cho S, Jo H, Jang S, Park J, Jung HJ, Yun CB, et al. Structural health monitoring of a cable-stayed bridge using wireless smart sensor technology: Data analyses. Smart Struct Syst 2010;6:461–80.

[19] Au SK. Assembling mode shapes by least squares. Mech Syst Signal Process 2011;25:163–79.

[20] Lam H-F, Zhang F-L, Ni Y-C, Hu J. Operational modal identification of a boat-shaped building by a Bayesian approach. Eng Struct 2017;138:381–93.

[21] Ni Y, Lu X, Lu W. Operational modal analysis of a high-rise multi-function building with dampers by a Bayesian approach. Mech Syst Signal Process 2017;86:286–307.

[22] Mevel L, Basseville M, Benveniste A, Goursat M. Merging sensor data from multiple measurement set-ups for non-stationary subspace-based modal analysis. J Sound Vib 2002;249:719–41.

[23] Döhler M, Mevel L. Modular subspace-based system identification from multi-setup measurements. IEEE Trans Automat Contr 2012;57:2951–6.

[24] Parloo E, Guillaume P, Cauberghe B. Maximum likelihood identification of non-stationary operational data. J Sound Vib 2003;268:971–91.

[25] Au S, Zhang F. Fast Bayesian ambient modal identification incorporating multiple setups. J Eng Mech 2012;138:800–15.

[26] Xie YL, Zhu YC, Au SK. Operational modal analysis of brodie tower using a Bayesian approach. UNCECOMP 2017 - Proc. 2nd Int. Conf. Uncertain. Quantif. Comput. Sci. Eng., 2017.

[27] Brownjohn JMW, Raby A, Au SK, Zhu Z, Wang X, Antonini A, et al. Bayesian operational modal analysis of offshore rock lighthouses: Close modes, alignment, symmetry and uncertainty. Mech Syst Signal Process 2019;133:106306.

[28] Zhang J, Prader ; J, Grimmelsman ; K A, Asce AM, Moon ; F, Aktan ; A E, et al. Experimental Vibration Analysis for Structural Identification of a Long-Span Suspension Bridge. AscelibraryOrg 2013;139:748–59.

[29] Siringoringo DM, Fujino Y. System identification of suspension bridge from ambient vibration response. Eng Struct 2008;30:462–77.

[30] Shi W, Shan J, Lu X. Modal identification of Shanghai World Financial Center both from free and ambient vibration response. Eng Struct 2012;36:14–26.

[31] Chen WH, Lu ZR, Lin W, Chen SH, Ni YQ, Xia Y, et al. Theoretical and experimental

modal analysis of the Guangzhou New TV Tower. Eng Struct 2011;33:3628–46.

[32] Li QS, Zhi LH, Tuan AY, Kao CS, Su SC, Wu CF. Dynamic behavior of Taipei 101 tower: Field measurement and numerical analysis. J Struct Eng 2011;137:143–55.

[33] Au SK. Fast Bayesian ambient modal identification in the frequency domain, Part I: Posterior most probable value. Mech Syst Signal Process 2012;26:60–75.

[34] Li B, Au SK. An expectation-maximization algorithm for Bayesian operational modal analysis with multiple (possibly close) modes. Mech Syst Signal Process 2019;132:490–511.

[35] Zhang FL, Au SK, Lam HF. Assessing uncertainty in operational modal analysis incorporating multiple setups using a Bayesian approach. Struct Control Heal Monit 2015;22:395–416.

[36] McLachlan GJ, Krishnan T. The EM Algorithm and Extensions: Second Edition. John Wiley & Sons; 2007.

[37] Wu CFJ. On the Convergence Properties of the EM Algorithm. Ann Stat 1983;11:95–103.

[38] Berlinet A, Roland C. Parabolic acceleration of the em algorithm. Stat Comput 2009;19:35–47.

[39] Berlinet AF, Roland C. Acceleration of the em algorithm: P-EM versus epsilon algorithm. Comput Stat Data Anal 2012;56:4122–37.

[40] Petersen KB, Pedersen MS. The Matrix Cookbook (version: November 15, 2012). 2012.

[41] Au SK. Fast Bayesian ambient modal identification in the frequency domain, Part II: Posterior uncertainty. Mech Syst Signal Process 2012;26:76–90.

[42] Au SK, Brownjohn JMW, Mottershead JE. Quantifying and managing uncertainty in operational modal analysis. Mech Syst Signal Process 2018;102:139–57.

[43] Siu-Kui Au, James Brownjohn, Binbin Li AR. Understanding and Managing Identification Uncertainty of Close Modes in Operational Modal Analysis. Mech Syst Signal Process 2020;accepted.

[44] Zhu Z, Au SK, Wang X. Instrument noise calibration with arbitrary sensor

orientations. Mech Syst Signal Process 2019;117:879–92.

[45] Brincker R, Zhang L, Andersen P. Modal identification of output-only systems using frequency domain decomposition. Smart Mater Struct 2001;10:441–5.

[46] Otto A. OoMA Toolbox (https://www.mathworks.com/matlabcentral/fileexchange/68657-ooma-toolbox). MATLAB Central File Exchange; 2020.